nature neuroscience

Article

https://doi.org/10.1038/s41593-026-02414-w

# Glutamate concentration tunes AMPA receptor function through conductance-state occupancy

Received: 9 June 2025

Accepted: 14 July 2026

Published online: 02 September 2026

Check for updates

Gokulakrishna Banumurthy[1,3], Reagan L. Pennock[1,3], Luke T. Coddington[1,2,3], Xiaohui Yan[1], Gabrielle N. Smith[1], Linda Overstreet-Wadiche[1] ✉ & Jacques I. Wadiche[1] ✉

α-amino-3-hydroxy-5-methyl-4-isoxazolepropionic acid receptors (AMPARs) mediate excitatory synaptic transmission across the brain and exhibit distinct modes of opening depending on how much glutamate is bound. Despite extensive work on AMPAR conductance states and subunit composition, whether changes in glutamate levels at and around synapses regulate AMPAR function is unknown. Here we show that glutamate concentration ([glutamate]) at mouse interneuron synapses governs key biophysical features of AMPARs that are commonly used to infer subunit composition. Lower [glutamate] reduces hallmark AMPAR properties, including current–voltage rectification, polyamine block and $Ca^{2+}$ permeability, highlighting a strong dependence of receptor function on synaptic [glutamate]. Recordings from isolated AMPARs combined with numerical simulations reveal differential spermine affinity across distinct conductance states and establish [glutamate], rather than solely subunit composition, as a key determinant of receptor behavior. These findings uncover a previously unrecognized mechanism through which the synaptic glutamate landscape dynamically shapes AMPAR signaling, broadening the framework for how excitatory input is encoded within neural circuits.

Fast synaptic communication in the mammalian brain is primarily mediated by glutamatergic α-amino-3-hydroxy-5-methyl-4-isoxazolepropionic acid receptors (AMPARs) that are composed of four subunits (GluA1–4). Glutamate binding to AMPARs generates single-channel currents with up to four conductance states. As each of the four subunits contains a glutamate binding site, it is generally agreed that the multiple conductance states relate to the number of individual subunits that are bound by agonist[1,2]. Structural studies confirm that AMPARs with different numbers of agonist-bound subunits exhibit different pore sizes that likely correspond to conductance states[3]; however, it is not clear how these multiple conducting states shape AMPAR function at synapses, where AMPARs are exposed to brief and heterogeneous glutamate waveforms rather than steady-state conditions. For example, even as activity-dependent AMPAR subunit trafficking is a well-recognized mechanism of synaptic plasticity, alterations in synaptic glutamate concentration ([glutamate]) via presynaptic mechanisms are also predicted to affect the unitary conductance of postsynaptic AMPARs[4]. Identifying the physiological role of the multiple AMPAR conductance states and their relationship to [glutamate] is therefore fundamental to understanding synaptic transmission and plasticity.

AMPARs form hetero- or homomeric receptors with a notable difference in function revolving around the GluA2 subunit. GluA2 subunits undergo post-transcriptional editing at the Q/R site that renders the

[1]Department of Neurobiology, University of Alabama at Birmingham, Birmingham, AL, USA. [2]Present address: Howard Hughes Medical Institute Janelia Research Campus, Ashburn, VA, USA. [3]These authors contributed equally: Gokulakrishna Banumurthy, Reagan L. Pennock, Luke T. Coddington. ✉e-mail: lwadiche@uab.edu; jwadiche@uab.edu

channel impermeable to $Ca^{2+}$, whereas GluA2-lacking AMPARs are $Ca^{2+}$-permeable[2]. $Ca^{2+}$-permeable AMPARs (CP-AMPARs) are intensely studied due to their involvement in many forms of synaptic plasticity, as well as pathologies[2,5]. Hallmark biophysical and pharmacological properties are widely used to discriminate the presence of CP- versus calcium-impermeable (CI)-AMPARs, which may exist along a continuum[6]. Notably, CP-AMPARs are sensitive to intracellular polyamines that act as open channel blockers, resulting in minimal outward current at membrane potentials from 0 to +50 mV (inward rectification). Rectification and sensitivity to polyamine-derived toxins are widely used to estimate the relative abundance of CI and CP-AMPARs. Auxiliary subunits also modulate AMPAR rectification, polyamine sensitivity and $Ca^{2+}$ permeability[6–10]. Even more fundamentally, it remains unclear how conductance state occupancy contributes to these properties during synaptic signaling. Although AMPAR conductance states and polyamine block have been extensively characterized under steady-state conditions, whether these properties are dynamically regulated during synaptic transmission has not been resolved. In particular, AMPAR $Ca^{2+}$ permeability is typically treated as a static property defined by subunit composition and pore structure. Here we address whether $Ca^{2+}$ permeability instead varies as a function of [glutamate] and waveform during nonequilibrium synaptic or spillover activation.

Native AMPARs are exposed to a wide range of [glutamate]s that are predicted to influence the number of subunits bound by glutamate (receptor occupancy). Following presynaptic release of a single vesicle, the cleft [glutamate] peaks in the low millimolar range and can reach ~12 mM following multivesicular release (MVR)[11–13]. Glutamate is typically cleared rapidly from the synaptic cleft by diffusion followed by reuptake from the extracellular space, but following high-frequency stimulation and at some specialized synapses, a gradual clearance of cleft [glutamate] can generate a slow component of postsynaptic AMPAR activation[14–18]. The [glutamate] immediately outside the synapse is estimated to peak at ~200 µM, highlighting a relevant concentration for spillover between synapses[9,19–22]. Ambient submicromolar [glutamate] maintained in the extracellular space may also increase in pathological conditions[23–25]. Here we use synaptic manipulations, two-photon (2P) $Ca^{2+}$ imaging and 2P glutamate uncaging, excised patches, GluA2 conditional knockout (cKO) and heterologous expression systems to show that AMPAR current–voltage rectification, polyamine block and $Ca^{2+}$ permeability depend on [glutamate], with lower concentrations reducing rectification and $Ca^{2+}$ permeability. These results show that the broad range of physiologically relevant [glutamate] dynamically regulates hallmark biophysical properties of AMPARs by biasing occupancy among conducting states with distinct spermine affinity and $Ca^{2+}$ permeability.

## Results

### Glutamate concentration shapes AMPAR properties

To understand how [glutamate] affects AMPAR properties, we first leveraged a cerebellar circuit where two afferent pathways generate distinct [glutamate] transients at AMPARs on molecular layer interneurons (MLIs). Glutamate released from climbing fibers (CFs) generates slow-rising and decaying spillover excitatory postsynaptic currents (EPSCs) mediated by a lower [glutamate] compared to EPSCs at parallel fiber (PF) synapses[22,26–29]. We recently showed that glutamate from CFs and PFs converge onto a common pool of synaptic CP-AMPARs[22]. Using multiple criteria to distinguish PF versus CF synaptic stimulation[28], we confirmed that CF-EPSCs are more effectively blocked by a low-affinity antagonist than PF-EPSCs, indicating that they are generated by a lower [glutamate] (Extended Data Fig. 1; CF, 70.8 ± 3.3% and PF, 51.5 ± 3.2% of control, $n = 5$ each, $P = 0.0028$ unpaired $t$-test). We then asked how this difference influences the unitary conductance of AMPARs. Peak-scaled nonstationary noise analysis revealed that the AMPAR conductance underlying CF-spillover EPSCs was lower than PF-EPSCs (Fig. 1a,b; CF, 9.8 ± 1.2 pS and PF, 22.8 ± 2.9 pS; $n = 9$, $P = 0.001$, paired $t$-test). Thus, as predicted, alterations in the [glutamate] in the synaptic cleft change the apparent unitary conductance of postsynaptic AMPARs[4].

Having established that variations in the synaptic [glutamate] can generate variations in AMPAR conductance, we asked what other biophysical properties are altered. We first focused on the rectification index (RI), a widely used biophysical signature that distinguishes between GluA2-containing and GluA2-lacking AMPARs[30]. In the presence of intracellular polyamines, an inwardly rectifying current–voltage (IV) relationship typically indicates the absence of GluA2 subunits, whereas a linear IV suggests the presence of GluA2-containing AMPARs. With an intracellular pipette containing the polyamine spermine (100 µM), PF-EPSCs showed the anticipated inward rectification (Fig. 1c,d; RI, 0.42 ± 0.02, $n = 34$) consistent with GluA2-lacking AMPARs[31]. Conversely, the IV of CF-spillover EPSCs was nearly linear, suggesting GluA2-containing CI-AMPARs (Fig. 1c,d; RI, 0.77 ± 0.03, $n = 31$; $P < 0.0001$, unpaired $t$-test). We repeated PF- and CF-EPSC rectification measurements using perforated patch to maintain the native intracellular [spermine] and found that PF-EPSCs and CF-EPSCs exhibit distinct RI (Fig. 1c,d and Extended Data Fig. 2; PF RI, 0.38 ± 0.08 and CF RI, 0.87 ± 0.04, $n = 4$ each; $P = 0.0015$, unpaired $t$-test). This suggests our use of 100 µM intracellular spermine (4 mM ATP) with whole-cell recordings is a close approximation of native intracellular [polyamine] in MLIs. Of note, differences in AMPAR rectification and unitary conductance between CF- and PF-EPSCs were preserved in physiological extracellular $Ca^{2+}$ (1.5 mM), indicating that these effects are not an artifact of elevated $Ca^{2+}$ conditions (Extended Data Fig. 3).

Differences in [glutamate] transients could result in varying degrees of AMPAR desensitization. Blocking desensitization with cyclothiazide (CTZ) potentiated CF-spillover EPSCs (233.6 ± 56.3%; $n = 7$, $P = 0.0156$) without significantly affecting PF-EPSCs (129.8 ± 10.0%; $n = 5$, $P = 0.0625$). Similar differences in unitary conductance and RI between CF- and PF-EPSCs were observed in the presence of CTZ (Extended Data Fig. 4), indicating that desensitization does not account for the lower conductance of spillover-evoked responses. Transmembrane AMPAR regulatory proteins (TARPs) are also well-known to affect receptor gating and reduce the affinity of the AMPAR for intracellular polyamines[7,32,33]. Consistent with a role of TARP γ-2 that is highly expressed in MLIs[34,35], the decay time of CF-EPSCs was significantly faster in TARP γ-2 knockouts (KOs) (CF γ-2$^{-/-}$, 2.1 ± 0.25 ms and CF wild-type (WT), 3.6 ± 0.21 ms, $n = 10$ and 9, $P = 0.0003$, two-tailed unpaired $t$-test); however, the difference in RI between CF- and PF-EPSCs persisted in TARP γ-2 KOs (Extended Data Fig. 5). Thus, neither differences in AMPAR desensitization nor the major AMPAR accessory protein in MLIs can explain [glutamate]-dependent rectification.

We also compared CF- and PF-EPSC sensitivity to 1-naphthyl acetyl spermine (NASPM), a commonly used blocker of CP-AMPARs[36,37]. Bath application of NASPM (50 µM) differentially blocked alternating PF-EPSCs and CF-EPSCs in the same MLIs (by 72.4 ± 4.4% versus 36.1 ± 5.8%, $n = 10$; Fig. 1e). On average, NASPM blocked PF-EPSCs by 73.5 ± 2.5% ($n = 22$) and CF-EPSCs by only 40.1 ± 4.0% ($n = 23$; Fig. 1f). The conventional interpretation of these results is that CF spillover is mediated primarily by GluA2-containing AMPARs, whereas PF-EPSCs are mediated by GluA2-lacking AMPARs; however, glutamate from CFs activates the same $Ca^{2+}$-permeable AMPARs found at PF synapses[22], and polyamines are activity-dependent channel blockers that are influenced by the degree of AMPAR activation[38]. Using 2P imaging and selective CF and PF activation, we found that despite the low rectification and minimal NASPM block typically associated with CI-AMPARs, CF-EPSCs elicited similar NASPM-sensitive $Ca^{2+}$ transients (CaTs) to PF-EPSCs (Fig. 1g)[22]. Additionally, there was no correlation between EPSC amplitudes and CaTs measured at individual sites (Fig. 1h). Together, these results suggest the intriguing possibility that synaptic [glutamate] dynamics contributes to fundamental AMPAR properties.

https://doi.org/10.1038/s41593-026-02414-w

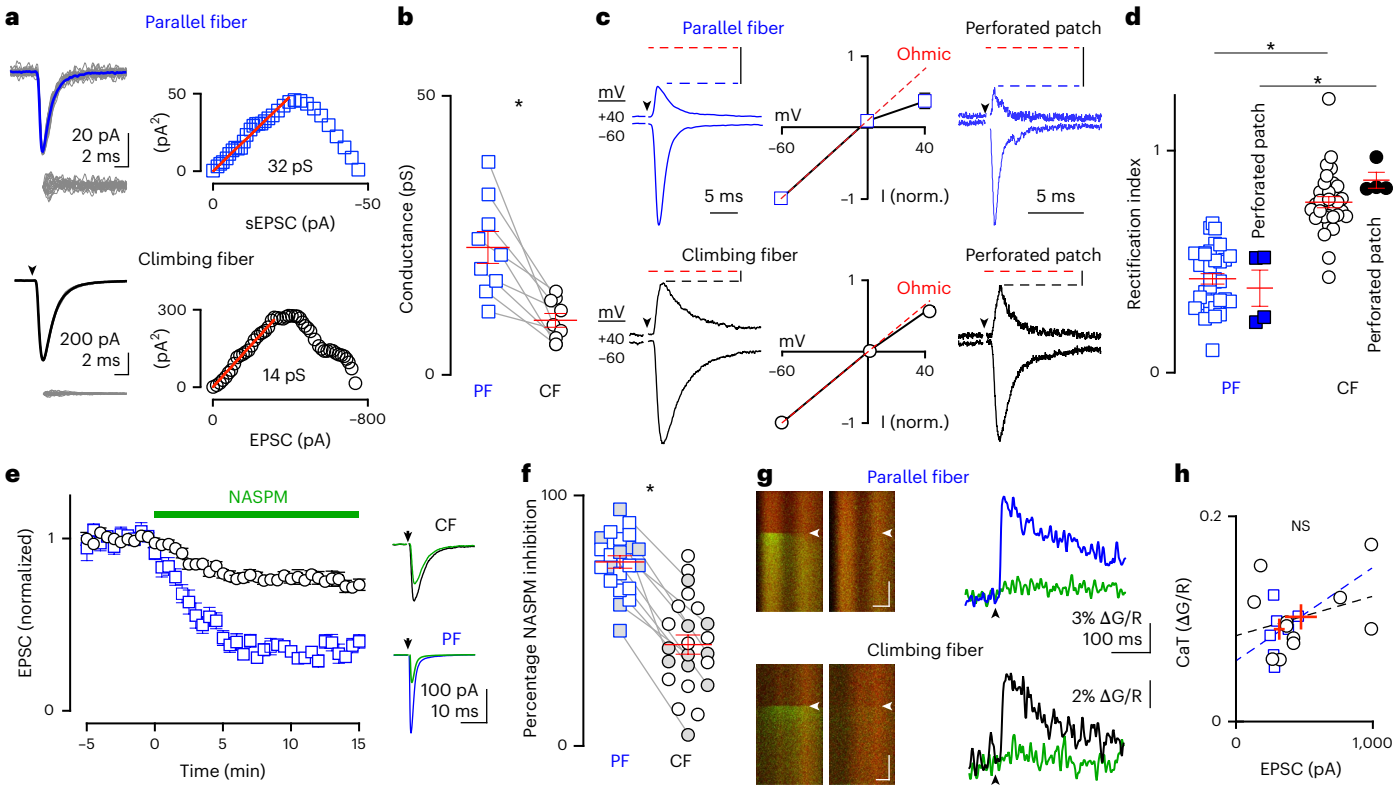


**Fig. 1 | Glutamate concentration shapes AMPAR properties. a**, Scaled average PF-sEPSCs (top, blue) and individual sweeps (20 sweeps; gray), difference currents (scaled average waveform minus each sweep), and variance-mean plot (blue squares, linear fit = 32 pS). Scaled average CF-EPSCs (bottom, black) and individual sweeps (20 sweeps; gray), difference currents, and variance-mean plot (black circles, linear fit = 14 pS). **b**, Summary of PF and CF unitary conductance (22.8 ± 2.9 and 9.8 ± 1.2 pS, respectively; $n = 9$; $P = 0.001$, two-tailed paired $t$-test). **c**, Example average PF- (blue, top) and CF- (black, bottom) EPSCs at −60 mV and +40 mV and corresponding IVs (left). Red dotted line indicates the predicted amplitudes for an ohmic (linear) response. Example average PF- (blue, top) and CF- (black, bottom) EPSCs at −60 mV and +40 mV recorded in the perforated patch configuration (right). **d**, Summary of RI of PF-EPSCs (0.42 ± 0.02, $n = 34$, blue empty squares), CF-EPSCs (0.77 ± 0.03, $n = 31$, black empty circles), perforated patch PF-EPSCs (0.38 ± 0.08, $n = 4$, blue filled circles), and perforated CF-EPSCs (0.87 ± 0.04, $n = 4$, black filled circles). One-way analysis of variance (ANOVA) ($P < 0.0001$) with Sidak post hoc tests ($P < 0.0001$). **e**, Average NASPM (50 µM) inhibition of PF- (blue squares, $n = 10$) and CF- (empty circles, $n = 10$) EPSCs. Inset shows representative PF- (blue) and CF- (black) EPSCs before and after NASPM application (green). **f**, Percent NASPM inhibition of PF- (blue squares) and CF- (black circles) EPSCs (73.5 ± 2.5%, $n = 22$ and 40.1 ± 4.0%, $n = 23$; $P < 0.0001$, two-tailed unpaired $t$-test). Ten cells were tested with both pathways (gray filled symbols and lines). **g**, Left side shows overlaid 2P line scans of red (Alexa 594, 30 µM) and green (Fluo-5F, 200 µM) channels following either PF or CF stimulation (arrow) in control (left) and in the presence of NASPM (right, 50 µM) (left). Scale: 50 ms, 1 µm. Right side shows corresponding CaTs (ΔG/R; Methods) following PF and CF stimulation before and in presence of NASPM (green). **h**, Lack of correlation of CaTs and EPSCs (PF blue $P = 0.5346$, $R^2 = 0.082$ and CF black $P = 0.3310$, $R^2 = 0.11$, Linear regression). NS, not significant. For all panels, summary data are mean± s.e.m. and Source Data are provided.

## [Glutamate] controls PF-EPSC rectification

To further test whether manipulating the synaptic [glutamate] can alter AMPAR rectification, we reduced the [glutamate] at PF synapses using the vacuolar-type ATPase blocker, bafilomycin (Baf; 1–5 µM). Baf eliminates the driving force for glutamate transport into synaptic vesicles, reducing quantal amplitude due to the release of empty and partially filled vesicles[39]. Baf robustly reduced the amplitude of PF-EPSCs and remaining EPSCs were fully blocked by NBQX, confirming that these low-amplitude responses are mediated exclusively by AMPARs (Fig. 2a,b). Baf also slowed the EPSC rise times consistent with a lower [glutamate] (Fig. 2c). Interestingly, Baf increased the RI of PF-EPSCs from 0.42 ± 0.03 to 0.56 ± 0.05, in concert with changes to amplitude and kinetics (Fig. 2d; $n = 7$ each, $P = 0.0041$, paired $t$-test). This shows that a presynaptic manipulation reducing the [glutamate] can influence the RI of synaptic AMPARs.

To manipulate the [glutamate] at a single population of postsynaptic receptors independent of presynaptic stimulation, we turned to 2P laser uncaging (2PLU). First, we visualized cell morphology and mapped the location of AMPAR clusters along MLI dendrites, where 2PLU generated AMPAR currents with amplitudes and kinetics similar to PF-EPSCs (Extended Data Fig. 6). Optimized AMPAR uncaging currents (uEPSCs) were generated near varicosities reflecting postsynaptic clusters (Fig. 3a, Extended Data Fig. 6). We then alternated the uncaging spot between the optimized location (near) and an orthogonal spot away from the dendrite (far), as shown in Fig. 3a. The 'far' stimulation site was displaced by ~0.5 µm relative to the 'near' site, a distance chosen to reduce local [glutamate] without attempting to replicate CF synaptic geometry, although a recent anatomical study indicates that CF release sites can be located within ~1 µm of PF synapses[40]. uEPSCs were evoked repeatedly at alternating sites at −60, 0 and +40 mV (Fig. 3b). uEPSCs generated at the far site had smaller amplitudes and slower rise times, suggesting that the same cluster of AMPARs was activated by a lower [glutamate] (Fig. 3b). The unitary conductances estimated for near (24.7 ± 2.2 pS) and far (14.7 ± 1.5 pS; $n = 5$) uncaging responses closely matched those measured for PF synaptic and CF-spillover EPSCs, indicating that reduced glutamate exposure alone is sufficient to shift AMPAR openings toward lower-conductance states. uEPSCs at the far uncaging spots had a higher RI than those at the near uncaging spots (Fig. 3c; 0.59 ± 0.05 and 0.45 ± 0.03, $n = 6$ each, $P = 0.0216$, paired $t$-test). We also performed experiments in which uEPSCs were evoked at different laser powers while keeping the uncaging location fixed at an optimized receptor cluster. When we reduced the

https://doi.org/10.1038/s41593-026-02414-w

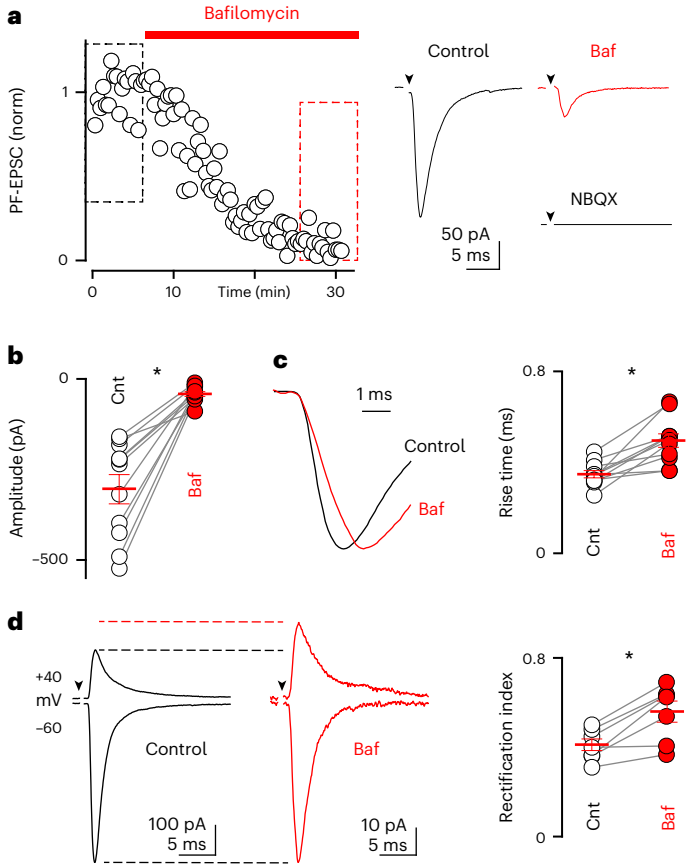


**Fig. 2 | [Glutamate] controls PF-EPSC rectification index. a**, Time course of PF-MLI EPSC amplitude evoked at 0.5 Hz and bath application of bafilomycin (1 µM). Right side shows average PF-EPSCs in control, Baf (1 µM) and NBQX (1 µM) at −60 mV, in the presence of R-CPP (5 µM) and picrotoxin (100 µM). EPSCs were not detected above baseline noise (3× baseline s.d.) following NBQX application ($n = 4/4$). **b**, Summary of average amplitude in control (−303.2 ± 40.5 pA), Baf (−41.3 ± 6.6; $n = 11$, $P \leq 0.0001$, two-tailed paired $t$-test). **c**, Normalized rising phase of control (black) and Baf (red) EPSCs and summary data of EPSC 20–80% rise times (control in black 0.35 ± 0.02 ms and bafilomycin 0.50 ± 0.03 ms in red; $n = 11$ each, $P = 0.0004$, two-tailed paired $t$-test). **d**, Normalized EPSCs (to −60 mV) recorded at −60 mV and +40 mV (left) during the periods represented by the boxes in **a**. RI summary (right) for control (0.42 ± 0.03) and Baf (0.56 ± 0.05); $n = 7$ each, $P = 0.0041$, two-tailed paired $t$-test. For all panels, summary data are mean ± s.e.m. and Source Data are provided.

laser power sufficiently to slow the uEPSC rise time, indicating a lower [glutamate], AMPAR RI increased (Fig. 3d–f). Together, these experiments show that reducing [glutamate] by reducing presynaptic vesicle content, or by adjusting uncaging laser location/power, increases AMPAR RI independent of changes in subunit composition.

## [Glutamate] generates a range of AMPAR rectification

To control precisely the [glutamate] and time course at AMPARs, we pulled outside-out excised patches from MLIs and used a piezo-driven theta pipette that allows rapid solution exchange (Fig. 4a). The RI of peak AMPAR currents generated by 200 µM glutamate was higher than the RI of currents generated by 10 mM glutamate (Fig. 4b,d; 0.52 ± 0.02 and 0.28 ± 0.01 $n = 9$ and 10, $P < 0.0001$). We also used voltage ramps in CTZ to prevent AMPAR desensitization and to measure AMPAR-mediated currents across a wide voltage range. CTZ slows deactivation and can influence other aspects of AMPAR gating[41–45], but these effects do not account for the glutamate-dependent changes in $Ca^{2+}$ permeability (see below) and rectification, which were observed with or without CTZ. Voltage ramps resulted in similar RIs compared to voltage jumps or [glutamate] jumps; and neither the speed (10–1,000 ms) nor direction of the ramp affected rectification (Extended Data Fig. 7). Voltage ramps in CTZ showed that AMPAR currents were strongly rectifying with high [glutamate] but became more linear with decreasing [glutamate] (Fig. 4c). On average, the RI shifted from 0.28 ± 0.03 at 10 mM glutamate to 0.81 ± 0.08 at 10 µM glutamate (Fig. 4d). We tested two to five different [glutamate]s per patch ($n = 14$), and in every case rectification tracked with [glutamate]. These results highlight that the same population of AMPARs show different degrees of rectification depending on [glutamate].

By suppressing desensitization, CTZ prolongs AMPAR currents during sustained or slow glutamate exposure, thereby increasing apparent glutamate affinity[19,41]. It is thus difficult to directly compare the [glutamate] in CTZ (Fig. 4c,d) to physiological [glutamate]s at postsynaptic receptors (1–12 mM) or outside of synapses (~200 µM)[11,12,19,46]; however, in the absence of CTZ (Fig. 4b,d), the ratio of the RI in 200 µM and 10 mM glutamate (0.52/0.28 = 1.86 ± 0.10) is similar to the ratio of the RI of CF- and PF-EPSCs (0.77/0.42 = 1.83 ± 0.11; Fig. 1d). This shows that the relative concentration-dependence of AMPAR rectification in patches can explain the difference in rectification at MLI synapses following CF and PF stimulation.

## [Glutamate] regulates AMPAR $Ca^{2+}$ permeability and influx

A fundamental property of AMPARs on interneurons is high $Ca^{2+}$ permeability[31,47]. Having established that [glutamate] controls both AMPAR conductance and rectification, we wondered whether [glutamate] also affects $Ca^{2+}$ permeability. To address this question, we compared the shifts in reversal potentials with partial replacement of external $Na^+$ with $Ca^{2+}$ (ref. 7,47). First, we used outside-out patches from MLIs to compare the reversal potential shift caused by ion replacement. With 1 mM glutamate, the high $Ca^{2+}$ solution did not significantly shift the reversal potential, as expected for receptors with high $Ca^{2+}$ permeability (Fig. 5a and ref. 7). Conversely, with 30 µM glutamate, the high $Ca^{2+}$ solution caused a hyperpolarizing shift in the reversal potential (Fig. 5b). We quantified this difference by calculating the shift in reversal potential between the high and low [glutamate]. In the $Na^+$ rich solution, both [glutamate]s resulted in similar reversal potentials (ΔErev = 0.1 ± 0.2 mV), yet in the $Ca^{2+}$ rich solution there was a significant difference between high and low glutamate (ΔErev = 6.9 ± 1.1 mV) (Fig. 5c). This shift indicates that 30 µM glutamate reduced the $Ca^{2+}$ permeability ($P_{Ca}/P_{Na}$) by ~30% compared to 1 mM glutamate (Fig. 5c). The results were similar whether intracellular spermine was excluded (Fig. 5a–c) or included (Fig. 5d–f). Together these results show that the $Ca^{2+}$ permeability of AMPARs depends on the [glutamate], with low [glutamate]s activating low conducting states that exhibit low $Ca^{2+}$ permeability.

To test whether the change in $Ca^{2+}$ permeability seen in patches also occurs at intact synapses, we compared CaTs associated with PF- and CF-EPSCs. As described by Pennock et al.[22], we identified sites on MLI dendrites where alternating minimal PF stimulation and CF stimulation generated overlapping EPSCs and CaTs indicating glutamate convergence to the same cluster of postsynaptic AMPARs (Fig. 5g–i). At these sites, the ratio of the CaT amplitude to EPSC charge integral was lower for CFs compared to PFs (Fig. 5j). Thus, the lower [glutamate] resulting from CF spillover seems to generate less $Ca^{2+}$ influx compared to the higher [glutamate] following PF stimulation, with the potential caveat that all-or-none CF-EPSCs, unlike minimal PF-EPSCs, can be generated from multiple postsynaptic clusters[22]. These results from outside-out patches and intact synapses show that $Ca^{2+}$ permeability and influx are dependent on [glutamate].

## AMPAR rectification depends on [glutamate] in GluA2cKO MLIs

Although occupancy of multiple conducting states is an attractive explanation for the results thus far, a potential confound is that the

https://doi.org/10.1038/s41593-026-02414-w

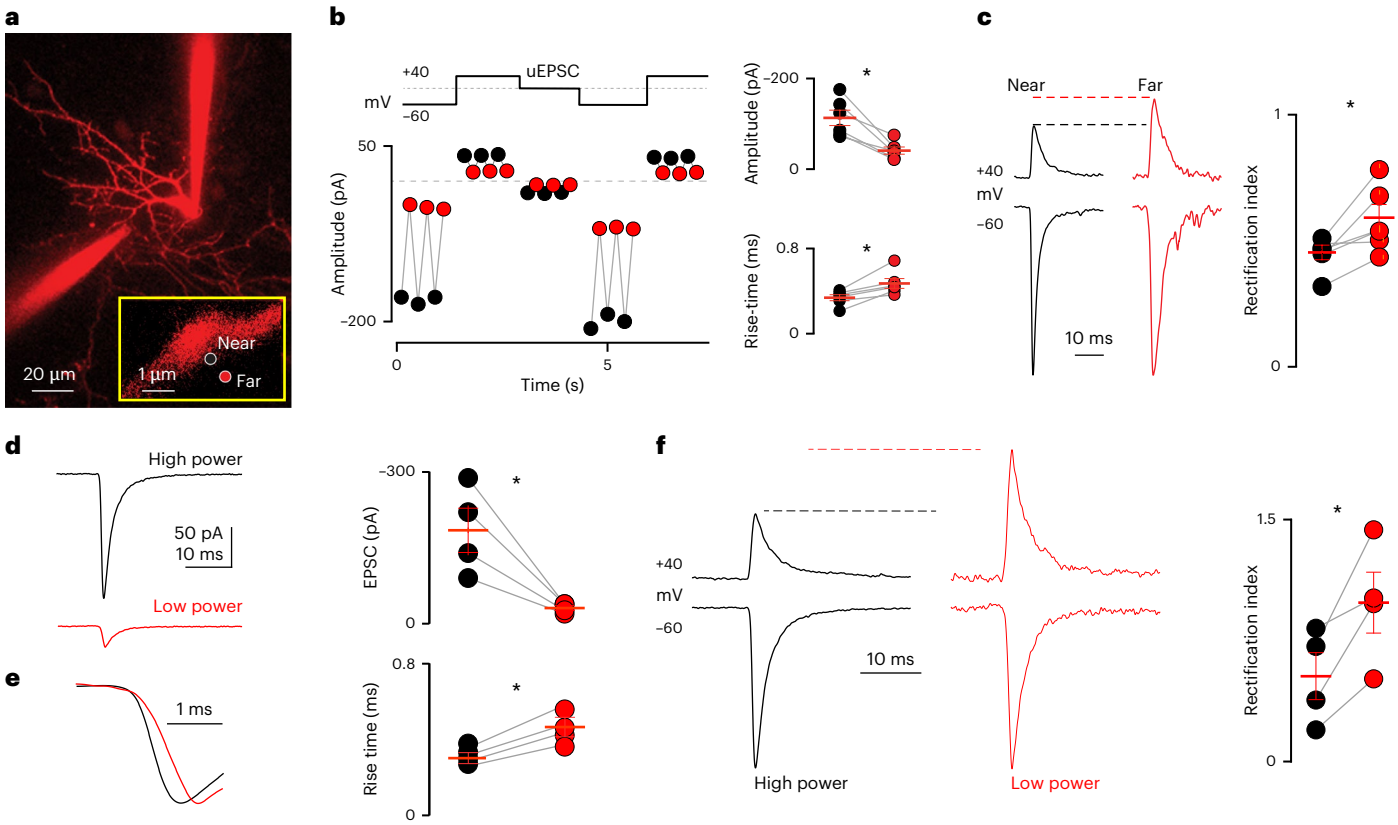


**Fig. 3 | [Glutamate] controls uncaging EPSC rectification. a**, 2P maximum *z*-projection of an MLI filled with Alexa 594 via the recording pipette. The stimulating electrode used to localize synaptic CaTs was also visualized with Alexa 594. Inset shows magnified region showing location of putative postsynaptic density and uncaging spots: near (0, black) and far (0.5 µm, red). **b**, Representative experimental protocol (left) for 2PLU measurement of uEPSCs at near (black) and far (red) spots. uEPSC peak amplitude and 20–80% rise time of uEPSC (right, at −60 mV) at near (−113.02 ± 17 pA, 0.34 ± 0.03 ms) and far uncaging spots (−40.9 ± 7.9 pA, 0.47 ± 0.05 ms; $n = 6$, $P = 0.005$ and 0.01, two-tailed paired *t*-tests). **c**, Representative normalized uEPSCs and summary RI at −60 and +40 mV at near (black, 0.45 ± 0.03) and far (red, 0.59 ± 0.05; $n = 6$, $P = 0.02$, two-tailed paired *t*-test) uncaging spots. **d**, Representative uEPSCs (−60 mV) and summary of uEPSC amplitude for high (black; 60–65 mW, −184.8 ± 44.1 pA, $n = 4$) and low (red; 30–40 mW, −29.8 ± 4.7 pA, $n = 4$, $P = 0.0298$, two-tailed paired *t*-test) laser power responses with 2P uncaging of MNI-glutamate (5 mM). **e**, uEPSCs rise phase from **d** and summary of the 20–80% rise times of uEPSCs evoked by high (black, 0.32 ± 0.02, $n = 4$) or low laser power (red, 0.45 ± 0.04, $n = 4$, $P = 0.0057$, two-tailed paired *t*-test). **f**, Representative normalized uEPSCs (−60 and +40 mV) and summary of RI evoked using high (black, 0.53 ± 0.14, $n = 4$) and low (red, 0.99 ± 0.19, $n = 4$, $P = 0.0343$, two-tailed paired *t*-test) laser power. For all panels, summary data are mean ± s.e.m. and Source data are provided.

[glutamate] dependence of AMPAR properties may result from AMPARs with different GluA2 subunit composition and thus conductance and polyamine sensitivity[2]. To address this possibility, we first repeated excised patch experiments (as in Fig. 4) using MLIs from GluA2cKO mice (PV-Cre;GluA2$^{flox/flox}$ mice). As expected, AMPAR currents from GluA2cKO patches exhibited strong rectification, confirming a contribution of GluA2 subunits to native AMPARs. With 100 µM intracellular spermine, there was no difference in the strong rectification generated by both a low (30 µM) and high (1 mM) [glutamate] (Fig. 6a); however, GluA2-lacking AMPARs have very high affinity for intracellular polyamines, with a half-maximal spermine blocking concentration of 0.3 µM (ref. 48). Thus, differences in [glutamate]-dependent rectification may only be evident under conditions when receptors are in the linear range rather than saturated by polyamines[48,49]. We reduced the intracellular [spermine] to either 30 µM or 2 µM to unmask [glutamate]-dependent rectification (Fig. 6a,b). With 2 µM intracellular spermine, the RI of GluA2-lacking AMPARs displayed a clear dependence on [glutamate], increasing from 0.59 ± 0.04 at 1 mM glutamate to 0.85 ± 0.05 at 30 µM glutamate (Fig. 6b). This suggests that [glutamate]-dependent rectification in GluA2-lacking AMPARs is qualitatively similar to WT AMPARs when receptors are not saturated by polyamines. Indeed, in the absence of intracellular spermine, GluA2-lacking AMPARs showed slight outward rectification with 1 mM glutamate (RI = 1.23 ± 0.02, $n = 4$) that was enhanced with 30 µM glutamate (RI = 1.83 ± 0.06, $n = 3$; $P = 0.007$, two-tailed unpaired *t*-test; Extended Data Fig. 8). Excised patches from WT MLIs also displayed rectification differences in the absence of intracellular spermine (Extended Data Fig. 8). This confirms that voltage-dependent gating at positive potentials is more stable at lower [glutamate], as previously shown[50,51]. Together these results demonstrate that spermine can occlude [glutamate]-dependent rectification, but that [glutamate]-dependent rectification does not require intracellular spermine.

We then revisited NASPM block and rectification of PF- and CF-EPSCs in GluA2cKO MLIs. The absence of GluA2 resulted in greater inhibition of EPSCs by NASPM compared to WT, with PF-EPSCs blocked by 85.6 ± 2.5% and CF-spillover EPSCs blocked by 82.3 ± 3.0% ($n = 3$, 4). This greater block confirms that a mixed population of CP and CI-AMPARs mediate transmission in WT MLIs. In GluA2cKOs, PF- and CF-EPSCs show strong and similar inward rectification (0.20 ± 0.02 and 0.21 ± 0.03, $n = 26$,13 respectively, Fig. 6c). However, reducing intracellular spermine to 2 µM again uncovered [glutamate]-dependent rectification, with greater rectification of PF-EPSCs (0.29 ± 0.05, $n = 8$) compared to CF-EPSCs (0.54 ± 0.09, $n = 10$; Fig. 6c,d). These results demonstrate that [glutamate]-dependent rectification does not result from a mixed population of GluA2-containing and GluA2-lacking AMPARs but can be masked by saturating intracellular [spermine].

https://doi.org/10.1038/s41593-026-02414-w

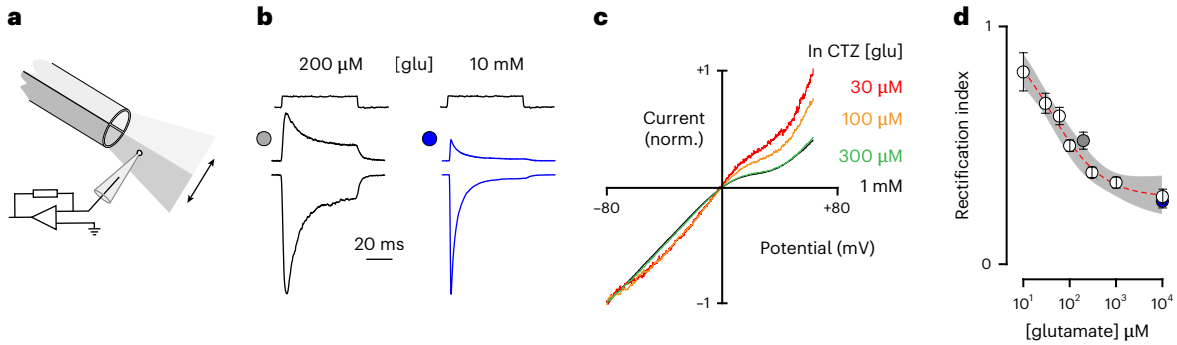


**Fig. 4 | [Glutamate] generates a range of MLI AMPAR rectification.** **a**, Cartoon of piezo-driven fast solution exchange recording configuration used in recordings of responses from outside-out (o/o) excised patches. **b**, Normalized peak-amplitude o/o MLI AMPAR responses (−60 and +40 mV) to a 50 ms application of 0.2 (gray) and 10 mM (blue) glutamate with desensitization intact. Solution exchange times (20–80 %) are shown above the traces and are typically less than 0.2 ms. The RI of peak responses (0.2 mM, 0.52 ± 0.02, $n = 9$; 10 mM, 0.28 ± 0.01, $n = 10$; $P < 0.0001$, two-tailed unpaired $t$-test) are plotted in **d**. **c**, IV plots of o/o MLI AMPAR currents (in 100 µM CTZ; normalized to −80 mV) following application of 30 (red), 100 (orange), 300 (green) and 1,000 µM (black) glutamate. **d**, Summary data of RI as a function of [glutamate]. On average, the glutamate-dependent RI was 0.81 ± 0.08 (10 µM, $n = 8$), 0.68 ± 0.04 (30 µM, $n = 10$), 0.62 ± 0.03 (60 µM, $n = 3$), 0.5 ± 0.02 (100 µM, $n = 5$), 0.39 ± 0.02 (300 µM, $n = 7$), 0.34 ± 0.02 (1 mM, $n = 14$) and 0.28 ± 0.03 (10 mM, $n = 5$). The RI as a function of [glutamate] is best fit with a half-maximum inhibitory concentration ($IC_{50}$) = 47.5 µM ($RI_{max}$ = 0.94, $RI_{min}$ = 0.29, Hill = −0.88, red dashed line). Solid gray and blue symbols represent RIs without CTZ (Fig. 4b). Gray area represents 95% CIs. For all panels, summary data are mean ± s.e.m. Source data are provided.

## AMPAR $Ca^{2+}$ permeability and influx depends on [glutamate] in GluA2cKO MLIs

To determine whether [glutamate]-dependence of $Ca^{2+}$ permeability is also independent of subunit composition, we repeated the relative $Ca^{2+}$ permeability measurements in patches and synapses from GluA2cKO MLIs (as in Fig. 5). In excised patches using 1 mM glutamate, the $Ca^{2+}$ rich solution did not shift the reversal potential whereas using 30 µM glutamate caused a significant hyperpolarizing shift in the reversal potential (Fig. 6e,f). Similar to WT patches, this shift indicates that 30 µM glutamate reduced the $Ca^{2+}$ permeability ($P_{Ca}/P_{Na}$) by ~30% compared to 1 mM glutamate (Fig. 6f). Likewise, we found that lower [glutamate] reduces $Ca^{2+}$ influx at synaptic GluA2-lacking AMPARs. We again identified sites on MLI dendrites where alternating minimal PF and CF stimulation generated overlapping CaTs, indicating glutamate convergence to the same cluster of postsynaptic AMPARs (Fig. 6g–i). At clusters of AMPARs that share input from PFs and CFs, lower [glutamate] from CF spillover generated less $Ca^{2+}$ influx compared to PF stimulation (Fig. 6g–j). Thus, lower [glutamate] results in lower relative $Ca^{2+}$ permeability in patches and $Ca^{2+}$ influx at synapses even in GluA2cKO MLIs.

## GluA1 AMPARs exhibit [glutamate]-dependent rectification and $Ca^{2+}$ permeability

TARPs regulate most aspects of AMPAR function, including glutamate affinity, rectification and desensitization[33]. To test whether [glutamate] dependent regulation of rectification and $Ca^{2+}$ permeability is an independent property of AMPARs or relies on TARPs or other factors, we repeated experiments in a minimal system using GluA1 expressed in HEK cells. We tested the RI of GluA1 in patches, while systemically varying both the [spermine] and [glutamate]. A high intracellular [spermine] of 100 µM produced strong rectification regardless of [glutamate] (Fig. 7a,b), consistent with saturation of the polyamine site[48]. Lowering intracellular spermine to 1 µM reduced rectification and began to reveal [glutamate] dependence, with 30 µM glutamate generating less rectification than higher [glutamate]s (Fig. 7a,b). At 0.2 µM intracellular spermine, rectification was highly sensitive to [glutamate] (Fig. 7a,b), with RIs that parallel those from GluA2cKO MLI patches (Fig. 7b).

We also tested whether [glutamate]-dependence of $Ca^{2+}$ permeability persisted in patches from GluA1 expressing HEK cells. Consistent with our results in MLIs from WT and GluA2cKO patches, 30 µM glutamate results in lower relative $Ca^{2+}$ permeability compared to 1 mM glutamate, either in the absence (Fig. 7c,e) or presence of spermine (Fig. 7d,e). Thus, [glutamate]-dependent regulation of rectification and $Ca^{2+}$ permeability is an intrinsic property of GluA1 AMPARs that does not require auxiliary proteins.

## AMPAR kinetic reaction scheme

To mechanistically understand the relationship between [glutamate] and voltage-dependent rectification, we developed a Markov model that incorporates many properties inherent to AMPARs. These include the multiple conductance states observed in single-channel recordings[1,4], intrinsic voltage-dependent channel opening[50,51], voltage-dependent spermine binding in the absence of agonist[38] and voltage-dependent spermine block and permeation[30,38] (Fig. 8a). In this scheme, the receptor (R) can bind up to four agonist (A) molecules (AR-$A_4$R = agonist binding states) that lead to four conductances (AO-$A_4$O = conducting states). Voltage-dependent binding of spermine (Sp) from the open state leads to spermine-dependent block (AOSp-$A_4$OSp = polyamine states). In addition, spermine can permeate at depolarized potentials ($k_{perm}$). Spermine can also bind the receptor in the absence of agonist (RSp) and then reach the spermine bound states with agonist (ARSp-$A_4$RSp = polyamine states). Our scheme is modeled after Bowie et al. and Robert & Howe[38,52] that assume the four subunits open independently (but see ref. 51). For simplicity, we also excluded desensitized states, as we fit this scheme with rectification values measured in the absence of desensitization. Simulations with this model show that variation in [glutamate] results in differential conducting state occupancies. At high [glutamate] (10 mM), the highest liganded states are reached with greatest frequency (Extended Data Fig. 9). Reducing [glutamate] to 1 mM decreases the occupancy of $A_4$X as $A_3$X and $A_2$X increase. Further reducing [glutamate] to 30 µM reveals that receptors are mostly unbound, with more frequent sojourns to the AX states (Extended Data Fig. 9). This difference in conducting state occupancy is similar to previous observations with single-channel studies[53].

Our model shows a similar glutamate dose–response curve as measured in patches from MLI recordings (Fig. 8b) as well as voltage-dependent rectification due to intracellular spermine (Fig. 8c). Notably, the simulations replicate the [glutamate] dependent rectification of steady-state IVs (Fig. 8d). An essential parameter of the model for replicating the experimental data is incorporation of proportional increases in spermine binding (Fig. 8a). Although the relationship between agonist binding and channel opening is complex, we propose increased spermine binding could arise as the channel's diameter widens with increasing number of agonists bound[3]. While the rates and IVs

https://doi.org/10.1038/s41593-026-02414-w

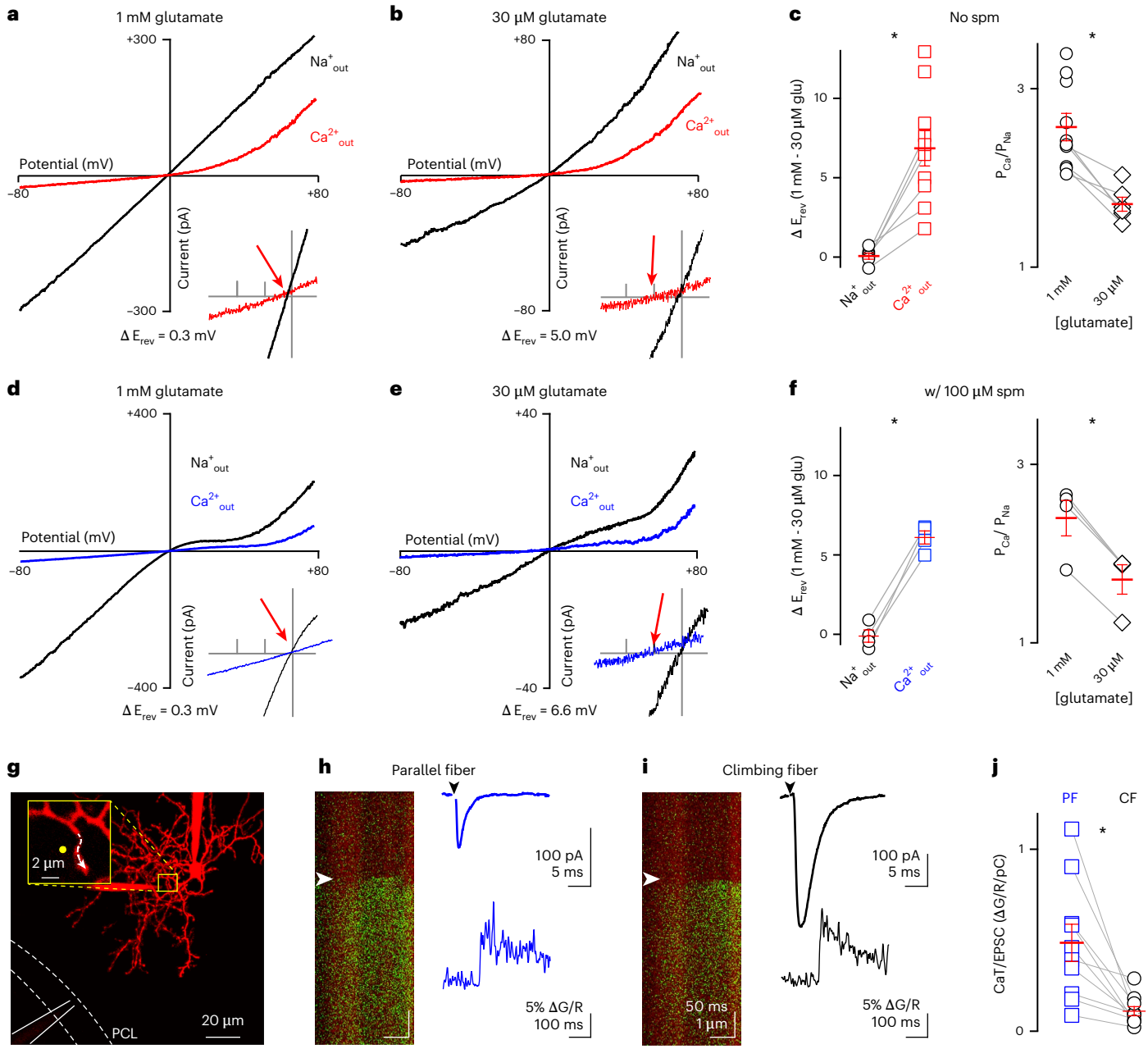


**Fig. 5 | [Glutamate] regulates AMPAR $Ca^{2+}$ permeability and influx.** **a**,**b**, Glutamate-dependent (1 mM and 30 µM) voltage ramps with $Na^+$ or $Ca^{2+}$-rich extracellular solution in the absence of intracellular spermine. Inset shows expanded scale of voltage ramps to show the shifts in reversal potentials (arrows). **c**, Summary of extracellular $Na^+$ rich reversal potential difference (1 mM to 30 µM; 0.08 ± 0.2 mV, $n = 6$) and extracellular $Ca^{2+}$ rich reversal potential difference (6.9 ± 1.1 mV, $n = 10$) and corresponding $P_{Ca}/P_{Na}$ (1 mM glutamate: 2.6 ± 0.15 and 30 µM glutamate: 1.7 ± 0.08, $n = 10$ and 6, $P = 0.003$ and 0.0026, two-tailed paired $t$-test with $n = 6$ for both). **d**–**f**, Same as **a**–**c** with 100 µM intracellular spermine. Extracellular $Na^+$ rich reversal potential difference (1 mM to 30 µM; −0.12 ± 0.4 mV, $n = 4$) and extracellular $Ca^{2+}$ rich reversal potential difference (6.1 ± 0.4 mV, $n = 4$) and corresponding $P_{Ca}/P_{Na}$ (1 mM glutamate, 2.4 ± 0.20 and 30 µM glutamate, 1.7 ± 0.16, $n = 4$ each, $P = 0.0009$ and 0.0005, two-tailed paired $t$-test). **g**, Maximum 2P $z$-projection of MLI filled with Alexa 594 (red with recording pipette) with location of stimulating electrodes (PF red near yellow box and CF white near Purkinje cell layer; PCL). Inset shows magnified box region showing dendritic line scans (white dotted line) and location of shared AMPAR cluster (yellow circle). **h**, Average line scan following PF stimulation with corresponding EPSC (top) and CaT (bottom). **i**, Average line scan following CF stimulation with corresponding EPSC (top) and CaT (bottom). **j**, Summary of CaT/EPSC ratio following PF (0.49 ± 0.1) and CF (0.11 ± 0.02, $n = 10$ each, $P = 0.0043$, two-tailed paired $t$-test) from Pennock et al.[22]. For all panels, summary data are mean ± s.e.m. and Source data are provided.

shown are optimized for native AMPARs in MLIs, the same scheme with adjusted rates can simulate data from MLI GluA2cKO and GluA1 HEK patches. For each set of rates, we systematically varied the [spermine] and [glutamate] to explore the complex relationship between RI and polyamine/glutamate concentrations (Fig. 8e). In each case, the red line illustrates how [glutamate] alters the RI for the experimentally relevant [spermine]. Blue lines highlight how [spermine] affects the RI for high (1 mM) and low (30 µM) glutamate.

In summary, we show that four conducting states with different spermine affinities can replicate our experimental observation of [glutamate] dependent rectification. Although we did not simulate relative $Ca^{2+}$ flux, we speculate that $Ca^{2+}$ permeability is also a result

https://doi.org/10.1038/s41593-026-02414-w

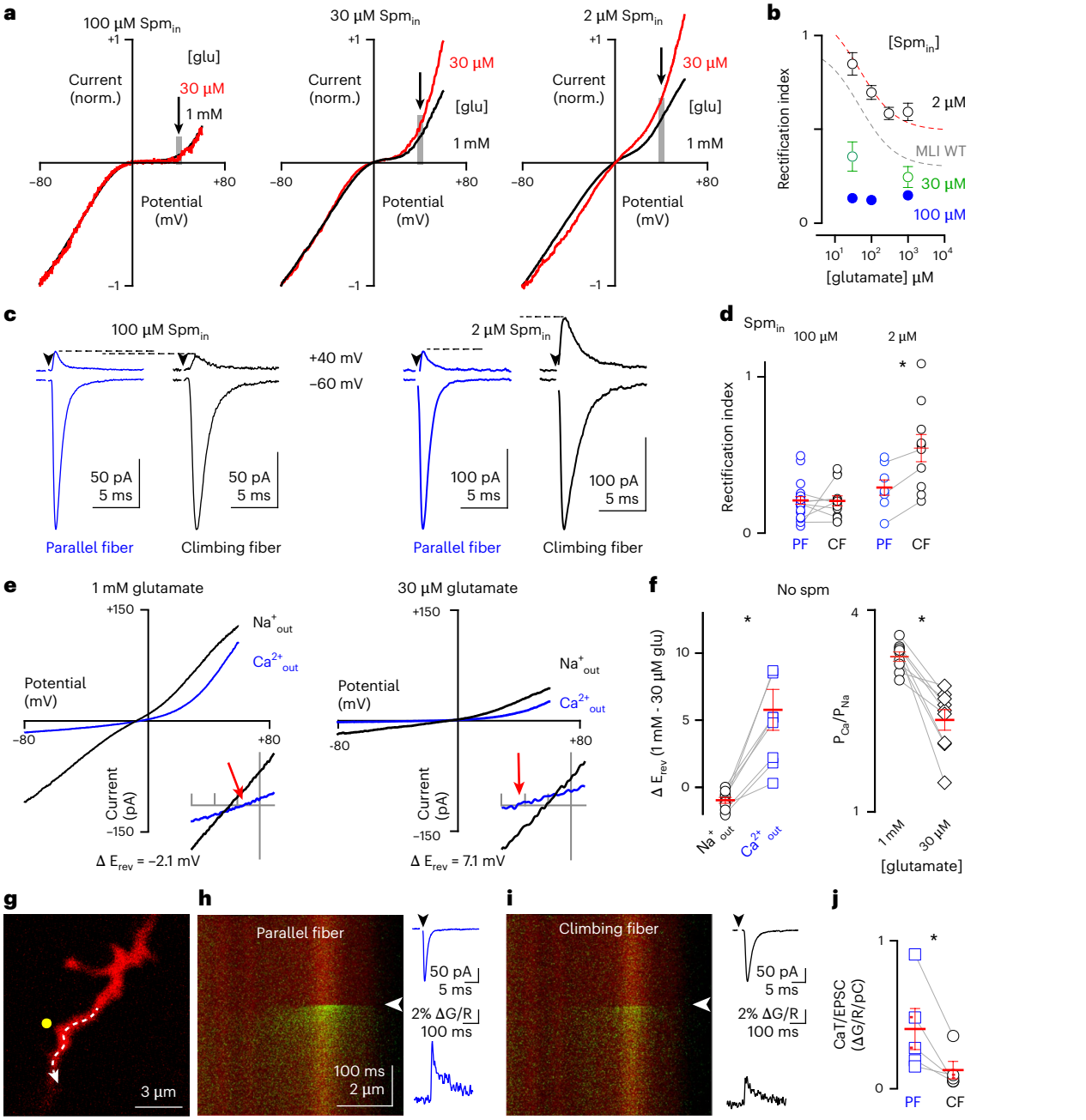


**Fig. 6 | GluA2cKO MLI rectification index, $Ca^{2+}$ permeability and $Ca^{2+}$/EPSC ratio. a**, Normalized glutamate-dependent voltage ramps (1 mM in black and 30 µM in red) with different internal spermine (100 µM, 30 µM and 2 µM). **b**, Summary data of RI as a function of [glutamate] from GluA2cKO o/o patches. With 100 µM spermine, the glutamate-dependent RI is 0.13 ± 0.007 (30 µM glutamate, $n = 4$), 0.12 ± 0.01 (100 µM glutamate, $n = 3$) and 0.14 ± 0.02 (1 mM glutamate, $n = 8$). With 30 µM internal spermine the RI is 0.35 ± 0.06 (30 µM glutamate, $n = 6$), 0.29 ± 0.01 (1 mM glutamate, $n = 6$). With 2 µM internal spermine, the RI is 0.85 ± 0.05 (30 µM glutamate, $n = 14$), 0.70 ± 0.03 (100 µM glutamate, $n = 10$), 0.58 ± 0.03 (300 µM glutamate, $n = 13$) and 0.59 ± 0.04 (1 mM glutamate, $n = 11$). With no spermine added, the RI is 1.7 ± 0.11 (30 µM glutamate, $n = 9$) and 1.1 ± 0.04 (1 mM glutamate, $n = 9$; Extended Data Fig. 8). The RI as a function of [glutamate] with 2 µM spermine is best fit with an $IC_{50} = 21.6$ µM ($RI_{max} = 1.2$, $RI_{min} = 0.56$, Hill = −1, red dashed line). The function describing the RI versus [glutamate] for WT MLI o/o (from Fig. 4) is shown in gray dashes for reference. **c**, PF- and CF-EPSCs (−60 mV and +40 mV) from GluA2cKO MLIs with 100 µM and 2 µM internal spermine. **d**, Summary data of RI from GluA2cKO EPSCs (**c**). With 100 µM spermine, the PF RI = 0.20 ± 0.02 ($n = 26$) and the CF RI = 0.21 ± 0.03 ($n = 13$). With 2 µM spermine, the PF RI = 0.29 ± 0.05 ($n = 8$) and the CF RI = 0.54 ± 0.09 ($n = 10$, $P = 0.03$, two-tailed unpaired $t$-test). **e**, Voltage ramps in the presence of 1 mM and 30 µM glutamate with $Na^+$- or $Ca^{2+}$-rich extracellular solution in the absence of intracellular spermine from GluA2cKO o/o patches. Inset shows expanded scale of voltage ramps to show the shifts in reversal potentials (arrows). **f**, Summary of $Na^+$-rich reversal potential difference (1 mM to 30 µM; −0.96 ± 0.2 mV, $n = 9$) and $Ca^{2+}$-rich reversal potential difference (5.8 ± 1.5 mV, $n = 9$) and corresponding $P_{Ca}/P_{Na}$ (1 mM glutamate, 3.3 ± 0.07 and 30 µM glutamate, 2.4 ± 0.15, $n = 9$ each, $P = 0.0043$ and 0.0007, two-tailed paired $t$-test). **g**, Magnified region showing dendritic line scans (white dotted line) and approximate location of shared AMPAR cluster (yellow circle). **h**, Average line scan following PF stimulation with corresponding EPSC (top) and CaT (bottom). **i**, Average line scan following CF stimulation with corresponding EPSC (top) and CaT (bottom). **j**, Summary of CaT/EPSC ratio following PF (0.40 ± 0.14) and CF (0.12 ± 0.06, $n = 5$ each, $P = 0.039$, two-tailed paired $t$-test) from GluA2cKO MLIs. For all panels, summary data are mean ± s.e.m. and Source data are provided.

https://doi.org/10.1038/s41593-026-02414-w

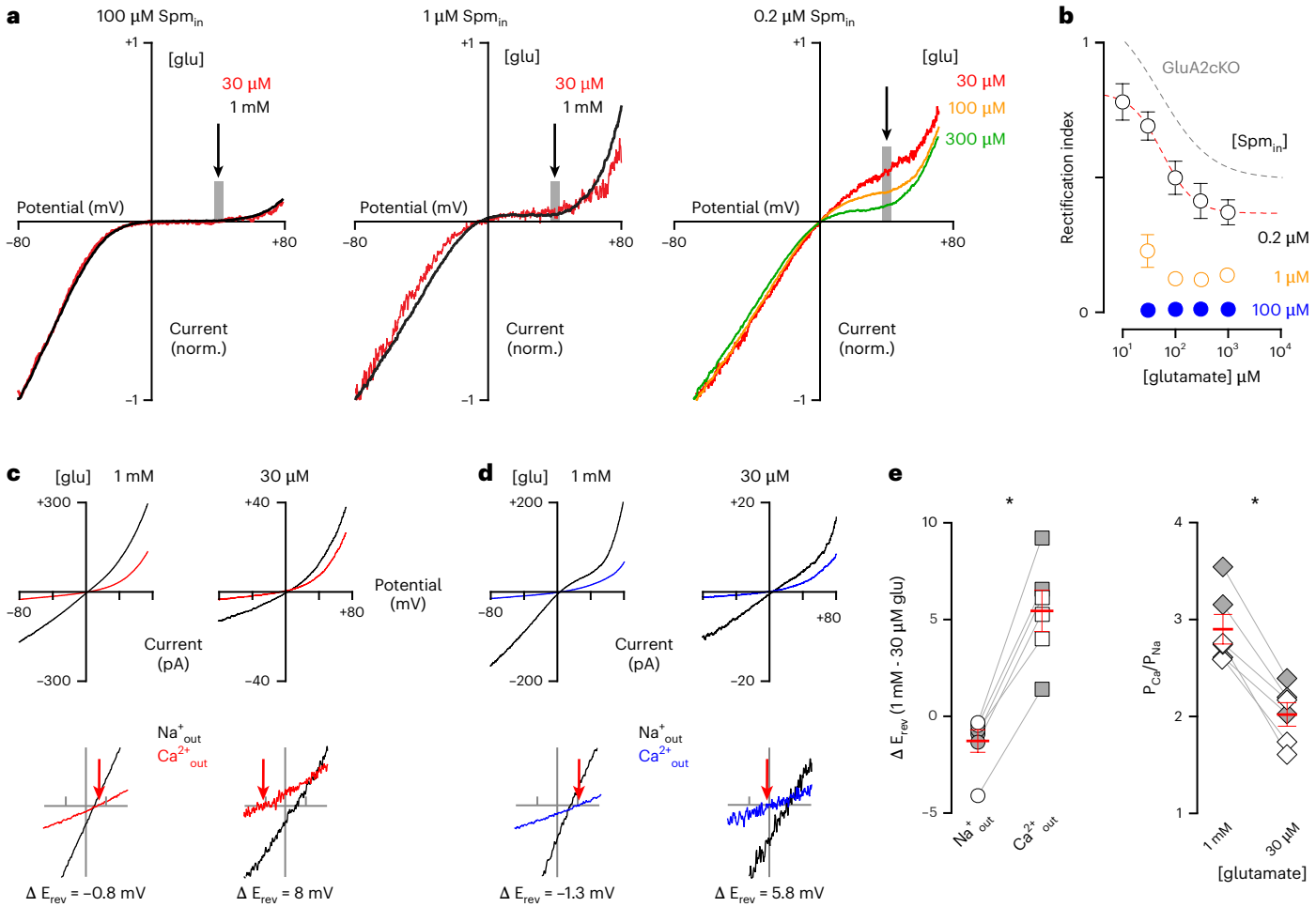


**Fig. 7 | GluA1-expressing HEK o/o excised patches. a**, Normalized glutamate-dependent voltage ramps with different internal spermine (100 µM, 1 µM and 0.2 µM). **b**, Summary data of RI as a function of [glutamate] from GluA1 HEK o/o patches. With 100 µM spermine, the glutamate-dependent RI is 0.01 ± 0.002 (30 µM glutamate, $n = 6$), 0.01 ± 0.002 (100 µM glutamate, $n = 3$), 0.012 ± 0.001 (300 µM glutamate, $n = 3$) and 0.01 ± 0.005 (1 mM glutamate, $n = 6$). With 1 µM internal spermine the RI is 0.23 ± 0.06 (30 µM glutamate, $n = 5$), 0.13 ± 0.03 (100 µM glutamate, $n = 3$), 0.12 ± 0.03 (300 µM glutamate, $n = 4$) and 0.14 ± 0.04 (1 mM glutamate, $n = 6$). With 0.2 µM internal spermine, the RI is 0.78 ± 0.07 (10 µM glutamate, $n = 3$), 0.69 ± 0.05 (30 µM glutamate, $n = 9$), 0.50 ± 0.06 (100 µM glutamate, $n = 7$), 0.41 ± 0.06 (300 µM glutamate, $n = 6$), 0.37 ± 0.06 (1 mM glutamate, $n = 10$). The RI as a function of [glutamate] with 0.2 µM spermine is best fit with an $IC_{50} = 56.6$ µM ($RI_{max} = 0.82$, $RI_{min} = 0.37$, Hill = −1.4, red dashed line). The function describing the RI versus [glutamate] for GluA2cKO o/o (from Fig. 6) is shown in gray dashes for reference. **c**, Voltage ramps in the presence of 1 mM and 30 µM glutamate with $Na^+$- or $Ca^{2+}$-rich extracellular solution in the absence of intracellular spermine. **d**, Voltage ramps in the presence of 1 mM and 30 µM glutamate with $Na^+$- or $Ca^{2+}$-rich extracellular solution in the presence of intracellular spermine. Inset shows expanded scale of voltage ramps to show the shifts in reversal potentials (arrows). **e**, Summary of $Na^+$-rich reversal potential difference (1 mM to 30 µM; −1.3 ± 0.6 mV, $n = 6$) and $Ca^{2+}$-rich reversal potential difference (5.4 ± 1.1 mV, $n = 6$) and corresponding $P_{Ca}/P_{Na}$ (1 mM glu, 2.9 ± 0.15 and 30 µM glu, 2.0 ± 0.12, $n = 6$ each, $P = 0.0002$ and 0.0004, two-tailed paired $t$-test with $n = 6$). Empty symbols denote 0 µM spermine and filled symbols have 0.2 µM added intracellular spermine. For all panels, summary data are mean ± s.e.m. and Source data are provided.

of differential occupancy of conducting states (Fig. 8f). More generally, these results show how the [glutamate]-dependent occupancy of multiple conducting states expands the functional diversity of AMPARs beyond the known contribution of subunit composition and auxiliary proteins.

## Discussion

Single-channel recordings and structural studies show that AMPARs exhibit multiple conductance states resulting from differing numbers of agonist-bound subunits[1,3,4]. We leveraged a circuit where two pathways generate distinct [glutamate] transients at a shared population of AMPARs to directly test how these differences regulate fundamental properties of native receptors. At MLI synapses, a low [glutamate] from CFs spills over to activate $Ca^{2+}$-permeable AMPARs that are also activated by higher [glutamate] from PFs[22]. Compelled by the paradox that spillover EPSCs show electrophysiology and pharmacology signatures typically assigned to $Ca^{2+}$-impermeable AMPARs, we investigated whether variations in [glutamate] confer diversity of AMPAR properties. These results support a model in which differential spermine affinity across multiple conducting states contributes to glutamate-dependent regulation of AMPARs previously attributed solely to subunit composition and auxiliary proteins.

### Native AMPARs are exposed to a range of [glutamate]

Following a single action potential, synaptic AMPARs experience a cleft [glutamate] in the 1–3 mM range that is cleared rapidly by diffusion and reuptake[11,54]. Higher peak [glutamate] can be achieved at synapses with MVR where several vesicles are released per active zone, producing estimated cleft concentrations of ~10 mM, a form of signaling prominent at rodent and human synapses[12,13,55–60]. Even at univesicular synapses, stimulus trains can generate complex [glutamate] transients due to a combination of presynaptic facilitation and delayed release

https://doi.org/10.1038/s41593-026-02414-w

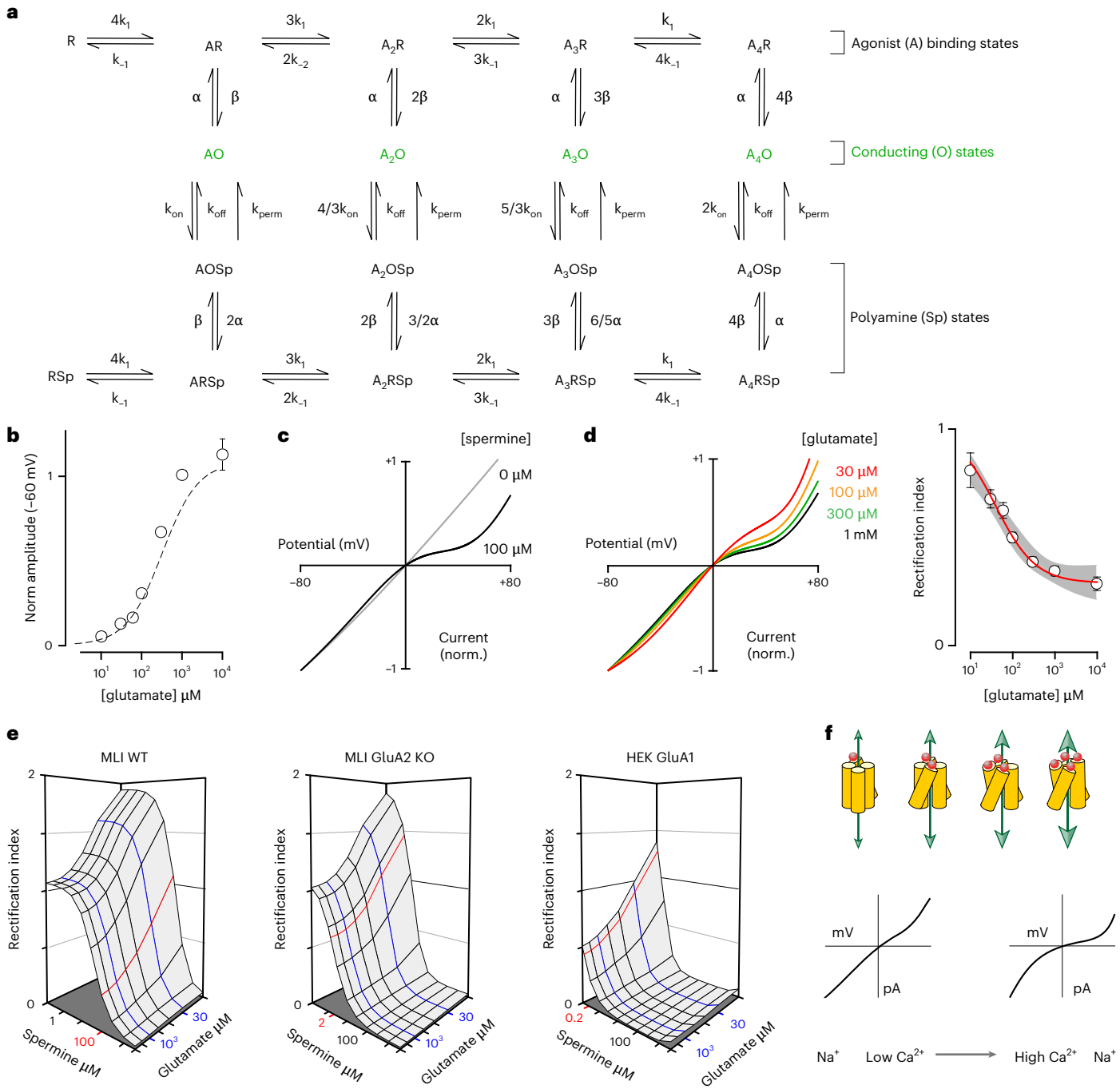


**Fig. 8 | Multiple conducting state AMPAR model. a**, Kinetic scheme of the AMPAR model used to fit AMPAR IV plots in o-o patches. Rates were as follows (units are $M^{-1}s^{-1}$ for rates denoted by * or $s^{-1}$). $k_1$*= $2 \times 10^7$, $k_{-1}$ = 9,000, β = 10,000, α = 3,000 exp(−V/120), $k_{on}$* = 0.75 exp(V/100), $k_{off}$ = 130 exp(−V/18), $k_{perm}$ = 8 exp(V/20), $k_i$ is dependent on [glutamate] and $k_{on}$ is dependent on [spermine]. Open states have conductances of 3, 9, 15 and 21 pS. V is the voltage in mV. **b**, Glutamate dose–response curve (normalized to 1 mM glutamate, −60 mV, $n$ = 15). 10 µM, 0.04 ± 0.02 ($n$ = 7), 30 µM, 0.12 ± 0.02 ($n$ = 10), 100 µM, 0.30 ± 0.05 ($n$ = 7), 300 µM, 0.66 ± 0.03 ($n$ = 8), 10 mM, 1.14 ± 0.12 ($n$ = 5). The half-maximum effective concentration ($EC_{50}$) = 421 µM ($I_{max}$ = 1.1, $I_{min}$ = 0, Hill = 1; dashed line). Data are shown as mean ± s.e.m. **c**, Simulated glutamate-dependent ramps in the absence or presence of 100 µM internal spermine. **d**, Simulated glutamate-dependent voltage ramps (30 µM, 100 µM, 300 µM and 1 mM glutamate). **d**, Overlaid plot of RI versus [glutamate] from numerical simulations (red line); $IC_{50}$ = 40.0 µM, $RI_{max}$ = 1, $RI_{min}$ = 0.29, Hill = −0.92) with data from MLI patch recordings (open circles). Data are shown as mean ± s.e.m. from Fig. 4d. **e**, Plots of RI as a function of glutamate and spermine concentration for o/o patches from WT MLI, GluA2cKO WT and GluA1 HEK. **f**, Cartoon and schematic of concentration-dependent rectification and $Ca^{2+}$ permeability.

that overwhelms clearance mechanisms and result in spillover[61,62]. In either case, a rapid mM glutamate transient is followed by a slower, lower-amplitude transient in the hundreds of micromolar range that acts on AMPARs both near and distant from release sites, respectively. The slower spillover transient has been estimated at ~200 µM, a subsaturating but still effective concentration for activating AMPAR responses[19,20,26–28,63]. Indeed, CF spillover onto MLIs engages a disinhibitory feedforward motif both in slices and in vivo[28,64]. At some specialized synapses, gradual clearance of cleft glutamate can also generate a slow component of AMPAR activation in the range of 10–100 µM that

shapes signaling[15–17]. Finally, the very low, submicromolar [glutamate] maintained in the extracellular space can also be regulated under pathological conditions[23–25]. Together, AMPARs in intact circuits experience a wide range of [glutamate] that are expected to produce differential receptor occupancy.

### Mechanisms of [glutamate]-dependent AMPAR properties

We show that AMPAR conductance states are not merely descriptive features of channel gating but instead function as dynamic regulators of $Ca^{2+}$ permeability during synaptic signaling. We first considered that glutamate-dependent effects could result from a mixed population of CP- and CI-AMPAR complexes, each with different affinities for glutamate. This is an essential consideration, as AMPAR subunits undergo activity-driven trafficking that can contribute to the wide range of rectification indices measured in EPSCs or excised patches[31,32]. Although a mixed population likely contributes to baseline variability in rectification, our results from GluA2cKO mice and homomeric GluA1 AMPARs demonstrate that even homogeneous populations of CP-AMPARs exhibit glutamate-dependent rectification and $Ca^{2+}$ permeability. Auxiliary proteins modulate nearly all aspects of AMPAR function, including conductance, rectification, polyamine sensitivity, and $Ca^{2+}$ permeability[5,6,33]. Yet we found that glutamate-dependent regulation of rectification and $Ca^{2+}$ permeability persists in the absence of the principal MLI TARP γ-2 and when GluA1 subunits are expressed in isolation. Thus, glutamate-dependent regulation of AMPAR properties is intrinsic to the receptor complex and does not require a specific auxiliary subunit. Because auxiliary subunits can bias conductance state occupancy, future work will be needed to determine whether specific TARPs modulate [glutamate]-dependent $Ca^{2+}$ permeability in GluA2-containing AMPARs[6].

The most parsimonious explanation for glutamate-dependent rectification is that it reflects differences in spermine affinity among AMPAR conducting states. Each AMPAR subunit contains a ligand-binding domain linked to the transmembrane pore that control channel gating, allowing each receptor to bind up to four agonists leading to multiple conductances[2,65]. We propose that as glutamate occupancy increases and higher conductance states are engaged, the pore becomes more permissive to intracellular spermine, resulting in greater spermine affinity. This is reflected in our model by assigning higher spermine affinity to the higher conducting states. Our results support the prediction that variation in synaptic [glutamate] generates different AMPAR conductance[4], although the precise relationship between agonist occupancy and the ion permeation pathway is still being resolved by functional and structural studies[3,66]. The critical requirement of our model is that different conducting states exhibit distinct spermine affinities; models with a single conducting state or with multiple states sharing identical spermine affinity could not reproduce our experimental results. Our simulations highlight the joint roles of intracellular spermine and glutamate concentrations in controlling rectification in both prototypic homomeric CP (GluA1) AMPARs as well as native heteromeric receptors.

Unexpectedly, we found that AMPAR $Ca^{2+}$ permeability itself depends on [glutamate] and that this effect can be explained by differential occupancy of AMPAR conductance states. We propose that glutamate-dependent $Ca^{2+}$ permeability results from state-dependent differences in $Ca^{2+}$ permeation, such that variable AMPAR occupancy engages conductance states with distinct pore geometry[3]. We further propose that TARP associations that influence conductance state occupancy in GluA2-containing AMPARs could also influence $Ca^{2+}$ permeability[6]. The model in Fig. 8 is not intended to represent a detailed structural mechanism but to provide a functional framework for how [glutamate] can shape AMPAR ion permeation. The model does not include desensitization states, a simplification justified by our observation that [glutamate]-dependent effects persist in CTZ.

Structural and functional studies indicate that AMPAR subconductance states reflect distributed conformational changes along the ion permeation pathway, including opening of the upper (M3) gate as well as dilation and stabilization of the selectivity filter formed by the M2 re-entrant loop at the Q/R site[3,67,68]. Recent work further demonstrates that physiological temperature promotes occupancy of higher conductance states (O3/O4) through enhanced dilation of the selectivity filter[69]. We found that glutamate-dependent regulation occurs at both room and near-physiological temperature. This region directly governs $Ca^{2+}$ permeability and polyamine block[3,67,68]. Notably, whereas rectification is related to spermine affinity, the glutamate-dependent effect on $Ca^{2+}$ permeability was independent of intracellular spermine. This suggests that lower [glutamate] bias receptors toward low-conductance open states that are less permissive to $Ca^{2+}$ flux. Because $Ca^{2+}$ is divalent and more strongly hydrated than $Na^{+}$, state-dependent changes in pore geometry and/or electrostatic stabilization would be expected to disproportionately reduce $Ca^{2+}$ flux. In other words, different conductance states likely reflect distinct conformations of the selectivity filter that differentially shape $Ca^{2+}$ permeation. While further work is required to define the underlying structural determinants, our functional results indicate that differences in $Ca^{2+}$ permeability can arise from biased occupancy of conductance states.

### Physiological significance

Our findings have functional consequences beyond the use of rectification as an assay for subunit composition. First, [glutamate]-dependence increases functional diversity by allowing a static population of AMPARs to dynamically vary current flux and relative $Ca^{2+}$ permeability independent of molecular changes. This endows postsynaptic compartments with the ability to distinguish glutamate released by the presynaptic partner from glutamate originating at more distant sources. Second, reduced $Ca^{2+}$ permeability at low [glutamate] may be protective, given the established association of CP-AMPARs with excitotoxicity under various pathological conditions[2]. Third, glutamate-dependent $Ca^{2+}$ permeability limits calcium influx during spillover, a signaling mode exhibited by many neural circuits[70]. Because spatiotemporal $Ca^{2+}$ transients direct different signaling outcomes[71], glutamate-dependent $Ca^{2+}$ permeability could link glutamate dynamics to distinct intracellular signaling cascades. Fourth, the ability to routinely identify CF-evoked CaTs at PF synapses mediated by a low [glutamate] indicates spillover is the predominant form of transmission between CFs and MLIs[22,40], despite recent assertions to the contrary based on rare anatomically defined synapses[72]. Finally, these results have potentially noteworthy implications for understanding the functional role of nanodomain organization at excitatory synapses, where alignments of pre- and postsynaptic elements are proposed to shape the spatiotemporal glutamate profile experienced by AMPARs[73]. Together, these findings provide new insight into the dynamic nature of synaptic communication and the multiple factors that influence AMPAR function in the brain.

## Online content

Any methods, additional references, Nature Portfolio reporting summaries, source data, extended data, supplementary information, acknowledgements, peer review information; details of author contributions and competing interests; and statements of data and code availability are available at https://doi.org/10.1038/s41593-026-02414-w.

## References

1. Rosenmund, C., Stern-Bach, Y. & Stevens, C. F. The tetrameric structure of a glutamate receptor channel. *Science* **280**, 1596–1599 (1998).
2. Hansen, K. B. et al. Structure, function, and pharmacology of glutamate receptor ion channels. *Pharmacol. Rev.* **73**, 298–487 (2021).

3. Yelshanskaya, M. V., Patel, D. S., Kottke, C. M., Kurnikova, M. G. & Sobolevsky, A. I. Opening of glutamate receptor channel to subconductance levels. *Nature* **605**, 172–178 (2022).
4. Smith, T. C. & Howe, J. R. Concentration-dependent substate behavior of native AMPA receptors. *Nat. Neurosci.* **3**, 992–997 (2000).
5. Cull-Candy, S. G. & Farrant, M. $Ca2^{+}$-permeable AMPA receptors and their auxiliary subunits in synaptic plasticity and disease. *J. Physiol.* **599**, 2655–2671 (2021).
6. Miguez-Cabello, F. et al. GluA2-containing AMPA receptors form a continuum of $Ca2^{+}$-permeable channels. *Nature* **641**, 537–544 (2025).
7. Soto, D., Coombs, I. D., Kelly, L., Farrant, M. & Cull-Candy, S. G. Stargazin attenuates intracellular polyamine block of calcium-permeable AMPA receptors. *Nat. Neurosci.* **10**, 1260–1267 (2007).
8. Carbone, A. L. & Plested, A. J. R. Superactivation of AMPA receptors by auxiliary proteins. *Nat. Commun.* **7**, 10178 (2016).
9. Lu, H.-W., Balmer, T. S., Romero, G. E. & Trussell, L. O. Slow AMPAR synaptic transmission is determined by stargazin and glutamate transporters. *Neuron* **96**, 73–80.e4 (2017).
10. McGee, T. P., Bats, C., Farrant, M. & Cull-Candy, S. G. Intracellular spermine is a key player in GSG1L's regulation of calcium-permeable AMPAR channel conductance and recovery from desensitization. *J. Neurosci.* **45**, e1930242025 (2025).
11. Clements, J., Lester, R., Tong, G., Jahr, C. & Westbrook, G. The time course of glutamate in the synaptic cleft. *Science* **258**, 1498–1501 (1992).
12. Wadiche, J. I. & Jahr, C. E. Multivesicular release at climbing fiber-Purkinje cell synapses. *Neuron* **32**, 301–313 (2001).
13. Holler, S., Köstinger, G., Martin, K. A. C., Schuhknecht, G. F. P. & Stratford, K. J. Structure and function of a neocortical synapse. *Nature* **591**, 111–116 (2021).
14. Rossi, D. J., Alford, S., Mugnaini, E. & Slater, N. T. Properties of transmission at a giant glutamatergic synapse in cerebellum: the mossy fiber-unipolar brush cell synapse. *J. Neurophysiol.* **74**, 24–42 (1995).
15. Kinney, G., Overstreet, L. & Slater, N. Prolonged physiological entrapment of glutamate in the synaptic cleft of cerebellar unipolar brush cells. *J. Neurophysiol.* **78**, 1320–1333 (1997).
16. van Dorp, S. & De Zeeuw, C. I. Variable timing of synaptic transmission in cerebellar unipolar brush cells. *Proc. Natl Acad. Sci. USA* **111**, 5403–5408 (2014).
17. Zampini, V. et al. Mechanisms and functional roles of glutamatergic synapse diversity in a cerebellar circuit. *ELife* **5**, e15872 (2016).
18. Balmer, T. S., Borges-Merjane, C. & Trussell, L. O. Incomplete removal of extracellular glutamate controls synaptic transmission and integration at a cerebellar synapse. *ELife* **10**, e63819 (2021).
19. Dzubay, J. & Jahr, C. The concentration of synaptically released glutamate outside of the climbing fiber-Purkinje cell synaptic cleft. *J. Neurosci.* **19**, 5265–5274 (1999).
20. Tsai, M.-C., Tanaka, K., Overstreet-Wadiche, L. & Wadiche, J. I. Neuronal glutamate transporters regulate glial excitatory transmission. *J. Neurosci.* **32**, 1528–1535 (2012).
21. Henneberger, C. et al. LTP induction boosts glutamate spillover by driving withdrawal of perisynaptic astroglia. *Neuron* **108**, 919–936.e11 (2020).
22. Pennock, R. L., Coddington, L. T., Yan, X., Overstreet-Wadiche, L. & Wadiche, J. I. Afferent convergence to a shared population of interneuron AMPA receptors. *Nat. Commun.* **14**, 3113 (2023).
23. Herman, M. A. & Jahr, C. E. Extracellular glutamate concentration in hippocampal slice. *J. Neurosci.* **27**, 9736–9741 (2007).
24. Kalivas, P. W. The glutamate homeostasis hypothesis of addiction. *Nat. Rev. Neurosci.* **10**, 561–572 (2009).
25. O'Donovan, S. M., Sullivan, C. R. & McCullumsmith, R. E. The role of glutamate transporters in the pathophysiology of neuropsychiatric disorders. *NPJ Schizophr.* **3**, 32 (2017).
26. Szapiro, G. G. & Barbour, B. B. Multiple climbing fibers signal to molecular layer interneurons exclusively via glutamate spillover. *Nat. Neurosci.* **10**, 735–742 (2007).
27. Mathews, P. J., Lee, K. H., Peng, Z., Houser, C. R. & Otis, T. S. Effects of climbing fiber driven inhibition on Purkinje neuron spiking. *J. Neurosci.* **32**, 17988–17997 (2012).
28. Coddington, L. T., Rudolph, S., Vande Lune, P., Overstreet-Wadiche, L. & Wadiche, J. I. Spillover-mediated feedforward inhibition functionally segregates interneuron activity. *Neuron* **78**, 1050–1062 (2013).
29. Malhotra, S. et al. Climbing fiber-mediated spillover transmission to interneurons is regulated by EAAT4. *J. Neurosci.* **41**, 8126–8133 (2021).
30. Bowie, D. & Mayer, M. L. Inward rectification of both AMPA and kainate subtype glutamate receptors generated by polyamine-mediated ion channel block. *Neuron* **15**, 453–462 (1995).
31. Liu, S. Q. & Cull-Candy, S. G. Synaptic activity at calcium-permeable AMPA receptors induces a switch in receptor subtype. *Nature* **405**, 454–458 (2000).
32. Jackson, A. C. & Nicoll, R. A. Stargazin (TARP γ-2) is required for compartment-specific AMPA receptor trafficking and synaptic plasticity in cerebellar stellate cells. *J. Neurosci.* **31**, 3939–3952 (2011).
33. Jackson, A. C. & Nicoll, R. A. The expanding social network of ionotropic glutamate receptors: TARPs and other transmembrane auxiliary subunits. *Neuron* **70**, 178–199 (2011).
34. Fukaya, M., Yamazaki, M., Sakimura, K. & Watanabe, M. Spatial diversity in gene expression for VDCCγ subunit family in developing and adult mouse brains. *Neurosci. Res.* **53**, 376–383 (2005).
35. Lein, E. S. et al. Genome-wide atlas of gene expression in the adult mouse brain. *Nature* **445**, 168–176 (2007).
36. Herlitze, S. et al. Argiotoxin detects molecular differences in AMPA receptor channels. *Neuron* **10**, 1131–1140 (1993).
37. Blaschke, M. et al. A single amino acid determines the subunit-specific spider toxin block of α-amino-3-hydroxy-5-methylisoxazole-4-propionate/kainate receptor channels. *Proc. Natl Acad. Sci. USA* **90**, 6528–6532 (1993).
38. Bowie, D., Lange, G. D. & Mayer, M. L. Activity-dependent modulation of glutamate receptors by polyamines. *J. Neurosci.* **18**, 8175–8185 (1998).
39. Zhou, Q., Petersen, C. C. & Nicoll, R. A. Effects of reduced vesicular filling on synaptic transmission in rat hippocampal neurones. *J. Physiol.* **525**, 195–206 (2000).
40. Santos-Valencia, F. et al. Climbing fibres recruit disinhibition to enhance Purkinje cell calcium signals. *Nature* **653**, 455–464 (2026).
41. Yamada, K. A. & Tang, C. M. Benzothiadiazides inhibit rapid glutamate receptor desensitization and enhance glutamatergic synaptic currents. *J. Neurosci.* **13**, 3904–3915 (1993).
42. Partin, K. M., Patneau, D. K., Winters, C. A., Mayer, M. L. & Buonanno, A. Selective modulation of desensitization at AMPA versus kainate receptors by cyclothiazide and concanavalin A. *Neuron* **11**, 1069–1082 (1993).
43. Trussell, L. O., Zhang, S. & Raman, I. M. Desensitization of AMPA receptors upon multiquantal neurotransmitter release. *Neuron* **10**, 1185–1196 (1993).
44. Koike-Tani, M., Saitoh, N. & Takahashi, T. Mechanisms underlying developmental speeding in AMPA-EPSC decay time at the calyx of Held. *J. Neurosci.* **25**, 199–207 (2005).
45. Fucile, S., Miledi, R. & Eusebi, F. Effects of cyclothiazide on GluR1/AMPA receptors. *Proc. Natl Acad. Sci. USA* **103**, 2943–2947 (2006).

46. Bergles, D. E. & Jahr, C. E. Synaptic activation of glutamate transporters in hippocampal astrocytes. *Neuron* **19**, 1297–1308 (1997).
47. Geiger, J. R. et al. Relative abundance of subunit mRNAs determines gating and $Ca2^{+}$ permeability of AMPA receptors in principal neurons and interneurons in rat CNS. *Neuron* **15**, 193–204 (1995).
48. Koh, D. S., Burnashev, N. & Jonas, P. Block of native Ca(2+)-permeable AMPA receptors in rat brain by intracellular polyamines generates double rectification. *J. Physiol.* **486**, 305–312 (1995).
49. Washburn, M. S., Numberger, M., Zhang, S. & Dingledine, R. Differential dependence on GluR2 expression of three characteristic features of AMPA receptors. *J. Neurosci.* **17**, 9393–9406 (1997).
50. Raman, I. M. & Trussell, L. O. Concentration-jump analysis of voltage-dependent conductances activated by glutamate and kainate in neurons of the avian cochlear nucleus. *Biophys. J.* **69**, 1868–1879 (1995).
51. Prieto, M. L. & Wollmuth, L. P. Gating modes in AMPA receptors. *J. Neurosci.* **30**, 4449–4459 (2010).
52. Robert, A. & Howe, J. R. How AMPA receptor desensitization depends on receptor occupancy. *J. Neurosci.* **23**, 847–858 (2003).
53. Gebhardt, C. & Cull-Candy, S. G. Influence of agonist concentration on AMPA and kainate channels in CA1 pyramidal cells in rat hippocampal slices. *J. Physiol.* **573**, 371–394 (2006).
54. Diamond, J. S. & Jahr, C. E. Transporters buffer synaptically released glutamate on a submillisecond time scale. *J. Neurosci.* **17**, 4672–4687 (1997).
55. Tong, G. & Jahr, C. E. Multivesicular release from excitatory synapses of cultured hippocampal neurons. *Neuron* **12**, 51–59 (1994).
56. Oertner, T. G., Sabatini, B. L., Nimchinsky, E. A. & Svoboda, K. Facilitation at single synapses probed with optical quantal analysis. *Nat. Neurosci.* **5**, 657–664 (2002).
57. Singer, J. H., Lassová, L., Vardi, N. & Diamond, J. S. Coordinated multivesicular release at a mammalian ribbon synapse. *Nat. Neurosci.* **7**, 826–833 (2004).
58. Christie, J. M. & Jahr, C. E. Multivesicular release at Schaffer collateral-CA1 hippocampal synapses. *J. Neurosci.* **26**, 210–216 (2006).
59. Rudolph, S., Overstreet-Wadiche, L. & Wadiche, J. I. Desynchronization of multivesicular release enhances Purkinje cell output. *Neuron* **70**, 991–1004 (2011).
60. Molnár, G. et al. Human pyramidal to interneuron synapses are mediated by multi-vesicular release and multiple docked vesicles. *Elife* **5**, e18167 (2016).
61. Kaeser, P. S. & Regehr, W. G. Molecular mechanisms for synchronous, asynchronous, and spontaneous neurotransmitter release. *Annu. Rev. Physiol.* **76**, 333–363 (2014).
62. Rudolph, S., Tsai, M.-C., von Gersdorff, H. & Wadiche, J. I. The ubiquitous nature of multivesicular release. *Trends Neurosci.* **38**, 428–438 (2015).
63. Matthews, E. A. et al. Optical analysis of glutamate spread in the neuropil. *Cereb. Cortex* **32**, 3669–3689 (2022).
64. Arlt, C. & Häusser, M. Microcircuit rules governing impact of single interneurons on Purkinje cell output in vivo. *Cell Rep.* **30**, 3020–3035.e3 (2020).
65. Coombs, I. D. & Cull-Candy, S. G. Single-channel mechanisms underlying the function, diversity and plasticity of AMPA receptors. *Neuropharmacology* **198**, 108781 (2021).
66. Shi, E. Y. et al. Noncompetitive antagonists induce cooperative AMPA receptor channel gating. *J. Gen. Physiol.* **151**, 156–173 (2019).
67. Twomey, E. C., Yelshanskaya, M. V., Grassucci, R. A., Frank, J. & Sobolevsky, A. I. Channel opening and gating mechanism in AMPA-subtype glutamate receptors. *Nature* **549**, 60–65 (2017).
68. Twomey, E. C., Yelshanskaya, M. V., Vassilevski, A. A. & Sobolevsky, A. I. Mechanisms of channel block in calcium-permeable AMPA receptors. *Neuron* **99**, 956–968.e4 (2018).
69. Kumar Mondal, A., Carrillo, E., Jayaraman, V. & Twomey, E. C. Glutamate gating of AMPA-subtype iGluRs at physiological temperatures. *Nature* **641**, 788–796 (2025).
70. Coddington, L. T., Nietz, A. K. & Wadiche, J. I. The contribution of extrasynaptic signaling to cerebellar information processing. *Cerebellum* **13**, 513–520 (2014).
71. Jędrzejewska-Szmek, J., Dorman, D. B. & Blackwell, K. T. Making time and space for calcium control of neuron activity. *Curr. Opin. Neurobiol.* **83**, 102804 (2023).
72. Park, C. et al. Synchronous climbing fiber activity enables instructive signaling for cerebellar learning through modulation of disinhibitory circuits. *Nat. Neurosci.* **29**, 1425–1438 (2026).
73. Biederer, T., Kaeser, P. S. & Blanpied, T. A. Transcellular nanoalignment of synaptic function. *Neuron* **96**, 680–696 (2017).

## Methods

All experimental preparations were performed using protocols approved by the Institutional Animal Care and Use Committee of the University of Alabama at Birmingham (IACUC-08767 and IACUC-21815). Mice were housed at room temperature (25 °C) with a 12-h light–dark cycle and humidity between 40 and 60%. Mice were provided ad libitum access to food and water.

### Genetic animal models

PV-GluA2cKO mice were generated by crossing PV-2A-Cre-D (no. 012358, The Jackson Laboratory) with GluR-B$^{2lox}$ mice (gift from R. Sprengel, Max Planck Institute). γ-2 KO mice (no. 001756, The Jackson Laboratory) were a gift from S. Tomita (Yale School of Medicine).

### Slice preparation

Parasagittal slices of the cerebellum were prepared from C57BL/6 male and female mice aged 16–38 days. Mice anesthetized using isoflurane (VetOne) were decapitated, and the cerebellum was removed in ice-cold cutting solution containing 110 mM CholineCl, 7 mM $MgCl_2$, 2.5 mM KCl, 1.25 mM $NaH_2PO_4$, 0.5 mM $CaCl_2$, 25 mM glucose, 11.5 mM Na-ascorbate, 3 mM Na-pyruvate and 25 mM $NaHCO_3$, bubbled with 95% $O_2$ and 5% $CO_2$. Mice > P27 also received intraperitoneal injection of 2, 2, 2-tribomoethanol (Avertin) followed by intracardial perfusion with cutting solution. The cerebellar vermis was mounted onto an agar block and sliced using a vibratome (270–300 µM; 7000-SMZ, Campden Instruments). The slices were incubated at 35 °C for 30 min in a solution containing 125 mM NaCl, 2.5 mM KCl, 1 mM $NaH_2PO_4$, 2.5 mM $CaCl_2$, 1.3 mM $MgCl_2$, 26.2 mM $NaHCO_3$ and 11 mM glucose. Unless noted, NMDARs were blocked with R-CPP (5 µM), $GABA_A$Rs were blocked with picrotoxin (100 µM). Key experiments were repeated in slices from P27-38 mice and datasets were pooled in Fig. 1c–f as results were similar.

### HEK cell expression

Transiently transfected HEK293T cells were used to express GluA1 AMPAR homomers (GluA1 flip splice variant in a pIRES2–EGFP expression vector obtained from the laboratory of S. Cull-Candy; Univ. College London). Key results were independently replicated using an additional rat GluA1 flip construct (pcDNA 3.1) obtained from the laboratory of S. Tomita (Yale Univ.). HEK293 cells were purchased from ATCC (American Type Culture Collection; CRL-3216). The cell line was checked against the International Cell Line Authentication Committee database of commonly misidentified cell lines, and was not listed. Cells were authenticated by ATCC before distribution; no additional authentication was performed for this study. HEK cells were grown in DMEM containing 10% FBS and 1% penicillin–streptomycin. At 60 to 80% confluency, cells were trypsinized and plated on glass coverslips (Fisher Scientific) that were treated with NaOH and coated with poly L-lysine. At 24 h post-splitting, the cells were transfected with 1.6 µg of GluA1 and 0.4 µg green fluorescent protein (GFP) using Lipofectamine (Invitrogen). At 6 h post-transfection, the medium was supplemented with 10–30 µM NBQX to prevent tonic activation of the receptors. Cells were used for recordings 24–48 h post-transfection. Outside-out patches were pulled from GFP-positive cells and recorded at room temperature. Patches with responses >500 pA to 1 mM glutamate were discarded to ensure voltage control.

### Electrophysiology

Whole-cell slice recordings were made at 33 ± 1 °C maintained with an inline heating device (Warner Instruments) using infrared contrast optics on an upright microscope (Olympus BX51). Recordings were made from identified MLIs located in the inner and middle thirds of the molecular layer. Recorded cells were located well below the slice surface so that diffusion and connectivity more closely resembled that of intact tissue. Responses were measured by a Multiclamp 700B amplifier (pClamp software, Molecular Devices), filtered at 2–5 kHz, and digitized at 15–50 kHz (Digidata 1440). Patch pipettes (BF150-110 or BF150-086, Sutter Instruments) were pulled (P-97, Sutter Instruments) to resistances between 2.5 and 5 MΩ. The series resistance ($R_s$), as measured by an instantaneous current response to a 1–10 mV step with the pipette capacitance canceled, was less than 25 MΩ and uncompensated. Data were discarded if $R_s$ changed (>20%). The intracellular pipette solution for voltage-clamp recordings contained 125 mM $CsMeSO_3$, 15 mM CsCl, 10 mM HEPES, 10 mM EGTA, 4 mM MgATP, 0.4 mM NaGTP and 5 mM QX314.

### Synaptic versus spillover stimulation

As previously described[28], we distinguished CF inputs from conventional PF inputs onto MLIs by multiple criteria: (1) adjusting the stimulating electrode position and intensity to evoke an all-or-none response, unlike responses after PF stimulation that were variable and graded[74]; (2) the paired-pulse ratio of CF-MLI responses (50-ms interstimulus interval), markedly depressed in contrast to PF responses that facilitated; and (3) CF-MLI EPSC kinetics were slower than those from PF synaptic connections.

### Patch experiments

A theta-glass flowpipe mounted on a piezo bimorph was used for agonist applications to outside-out patches. Patch experiments were performed at room temperature (25 ± 1 °C). Nucleated patches from MLIs were obtained following breakthrough by applying negative pressure and pulling the membrane-enveloped nucleus out of the slice. Intact nucleated patches were characterized by maintenance of high $R_{in}$ (GΩ seal) and the appearance of a spherical smooth bleb at the tip of the pipette. For fast solution exchange experiments, excised outside-out patches were used. Exchanged (20–80%) times were measured after each experiment by rupturing the patch and recording junction currents across the open pipette tip (<200 µs). A multiline manifold was used with the theta-glass for testing multiple solutions and concentrations to the same patch. Excised outside-out patches were placed in front of the control side of the flowpipe, and the protocol consisted of holding the patch at hyperpolarized potentials (−80 mV) for 250–350 ms before ramping the potential to +80 mV at a speed of 2 mV ms$^{-1}$ unless otherwise noted. This was repeated with the patch in front of the agonist side of the pipette before alternating back to the control side. Ramps were repeated every 3–5 s, and the responses to glutamate were subtracted from control to isolate the AMPAR response. An average of 10–40 sweeps were collected for each condition.

### Rectification index

CFs and PFs were stimulated using theta-glass pipettes while holding MLIs at −60, 0 and +40 mV to measure the RI in synaptic experiments. CFs were stimulated at a frequency of 0.1 Hz, and the PFs were stimulated at 0.2–0.5 Hz. An average of 10–20 sweeps were collected at each holding potential. Currents at 0 mV were subtracted from the currents at −60 and +40 mV to produce the traces used in the figures. The RI was calculated by comparing the ratio of currents at +40 mV to that of −60 mV, while dividing by the potential to correct for the changes in driving force.

$$RI = ((I_{+40mV}\text{-}I_{0mV})/+40)/((I_{-60mV}\text{-}I_{0mV})/-60).$$

### Peak-scaled nonstationary noise analysis

Spontaneous EPSCs (sEPSCs) from PFs were analyzed to minimize effects of spillover between neighboring PF-MLI synapses. EPSCs were detected using a derivative threshold (−50 pA ms$^{-1}$) and were used for analysis when there was at least 50 ms before subsequent events. CF-MLI EPSCs were evoked via electrical stimulation as previously described[22]. Events were acquired at 20 kHz and filtered at 1 kHz using a low pass Gaussian filter. For each experiment, events were aligned at 20% of the peak amplitude then averaged to produce

an average EPSC waveform. The average EPSC waveform was normalized to the amplitude of each event at the timepoint where the peak of the average waveform occurred then subtracted to produce a difference current. Difference currents from the decay phase were divided into 50 bins, each representing a 2% decrement from the peak of the average EPSC waveform, then averaged and squared to calculate variance. Variance was plotted against the amplitude of the average EPSC waveform corresponding to each bin. Single-channel AMPAR conductance from the limiting slope (single-channel current) of the first data points of each mean-variance plot were converted to conductance ($V_H$ = −60 mV).

### Perforated patch

The internal recording solution contained 140 mM CsCl, 4 mM $MgCl_2$, 10 mM EGTA, 10 mM HEPES, 0.03 mM Alexa 594 and Amphotericin B (Abcam; product no. AB141199, lot no. APN24046). In brief, Amphotericin B was dissolved in dimethylsulfoxide (DMSO; 60 mg $ml^{-1}$) then diluted to a final concentration of 300 µg $ml^{-1}$ in the internal recording solution[75,76]. Perforated patch recordings were made at room temperature (25 ± 1 °C). Seal resistance was >10 GΩ, and routinely >20 GΩ. After a seal was formed, access was monitored via a −10-mV test pulse delivered at a rate of 0.2 Hz. Steady-state series resistance was 30–50 MΩ. Recordings were discarded if the neuronal membrane ruptured before completion of the experiment, as indicated by (1) an abrupt decrease in series resistance and/or (2) filling of the soma with Alexa 594 (Extended Data Fig. 2).

### Calcium permeability

Excised outside-out patches from slices and GluA1-transfected HEK cells were perfused with the extracellular solution containing 125 mM NaCl, 2.5 mM KCl, 1 mM $NaH_2PO_4$, 26.2 mM $NaHCO_3$, 11 mM glucose, 2.5 mM $CaCl_2$ and 1.3 mM $MgCl_2$. Nucleated patches from MLIs and patches from HEK cells were exposed to one of two extracellular solutions: (1) $Na^+_{out}$ ($Na^+$ rich) solution contained 145 mM NaCl, 2.5 mM KCl, 1 mM $CaCl_2$, 1 mM $MgCl_2$, 10 mM HEPES, pH 7.4 (NaOH) or (2) $Ca^{2+}_{out}$ ($Ca^{2+}$ rich) solution contained 110 mM NMDG, 30 mM $CaCl_2$, 10 mM HEPES, pH to 7.4 with HCl, sucrose was added to match osmolarity of control solution. Tetrodotoxin (TTX; 1 µM), Picrotoxin (PTX; 100 µM) or SR-95531 (5 µM), and R-CPP (20 µM) were added to experiments in slices to isolate the AMPAR response. Cyclothiazide (CTZ; 100 µM) was added to prevent desensitization of AMPARs. The internal solution used for these recordings contained 100 mM CsCl, 35 mM CsF, 10 mM EGTA, 10 mM HEPES, 4 mM MgATP, 0.4 mM NaGTP and 5 mM QX314. The flowpipe used for solution exchange was mounted onto a piezoelectric device, triggered using a TTL pulse. AMPAR $P_{Ca}/P_{Na}$ (relative $Ca^{2+}$ permeability) was measured by comparing the reversal potentials ($E_{rev}$) in different external solutions ($Na^+_{out}$ rich versus $Ca^{2+}_{out}$ rich). The IV responses were fitted with multiorder polynomials, from which the interpolated reversal potential was calculated. The relative permeability $P_{Ca}/P_{Na}$ was determined using the equation:

$$P_{Ca}/P_{Na} = 1/4 \times a_{Na}/a_{Ca}(\exp^{[(2VCaErev-VNaErev)F/RT]} + \exp^{[(VCaErev-VNaErev)F/RT]})$$

where $a_{Na}$ and $a_{Ca}$ represent the activities of $Na^+$ and $Ca^{2+}$ in the extracellular solution. R, T and F have their conventional meaning. We tested two values for $a_{Na}$ and $a_{Ca}$: 0.75 and 0.55 (ref. 47) and 0.87 and 0.64 (ref. 7). The values for $E_{rev}$ were corrected for liquid junction potential values of 7.9 mV in $Na^+$ solutions and 13.4 mV in $Ca^{2+}$ solutions determined empirically as well as with LJPcalc 1.2 (PClamp, Molecular Devices).

### Two-photon $Ca^{2+}$ imaging

The internal recording solution for simultaneous 2P imaging and electrophysiological recording contained 100 mM $CsMeSO_3$, 50 mM CsCl, 10 mM HEPES, 1 mM $MgCl_2$, 2 mM MgATP, 0.3 mM NaGTP, 5 mM QX314, 0.03 mM Alexa 594 and 0.2 mM Fluo-5F. Two-photon excitation was achieved using a Chameleon Vision or Ultra II pulsed Ti:Sapphire lasers (Coherent) tuned to 810 nm for simultaneous imaging of cell morphology (Alexa 594) and $Ca^{2+}$ influx (Fluo-5F). Laser power was modulated via a Pockels cell (Model 350-80 Electro-Optic Modulator, ConOptics). Images were acquired on an Olympus BX51WI microscope equipped with a ×60 1.0 NA objective (Olympus). The point spread function of the system at 810 nm was measured using green 100-nm diameter beads (Tetraspeck Microspheres, Invitrogen). The full width at half-maximum of the point spread function was 445 ± 11 nm laterally and 1,893 ± 102 nm axially ($n$ = 6)[22]. Pairs of photomultiplier tubes (PMTs) collected light from epi- and trans-fluorescence pathways. Both pathways contained a 565-nm long pass beam splitter (565lxpr; Chroma), a GaAsP PMT (H7422P-40; Hamamatsu) with a 525/50 bandpass filter (ET525/50m; Chroma), and a multi-alkali PMT (R3896; Hamamatsu) with a 595/50 bandpass filter (ET595/50m; Chroma). Prairie View software (Bruker Corporation) was used for acquisition of imaging data. Imaging experiments involving CF stimulation (Figs. 1g,h, 5g–j and 6g–j) were performed in slices from P27-38 mice, when CF responses are large to facilitate identification of overlapping CF and PF $Ca^{2+}$ sites (as in ref. 22).

### Quantification of $Ca^{2+}$ transients

Imaging was initiated after at least 10 min of whole-cell dialysis to allow Alexa 594 and Fluo-5F to equilibrate. After isolating a CF or PF-EPSC sequential frame scanning occurred at 2–5 Hz while visually inspecting for increased Fluo 5F fluorescence coincident with evoked EPSCs. PF-evoked CaTs were easily localized below the stimulating electrode, while CF-evoked CaTs were more difficult to localize and occurred throughout the MLI dendritic arbor. A potential limitation of using $Ca^{2+}$ imaging to localize synaptic sites is that the spatial extent of $Ca^{2+}$ signals can overestimate the spread of receptor activation as a result of the $Ca^{2+}$ indicator diffusing from the initial receptor 'point source', as all $Ca^{2+}$ indicators act as mobile buffers that can shuttle calcium along the dendrite. We minimized this possibility by using low-affinity dyes and our estimates of spatial compartmentalization are consistent with previous reports[22,77,78]. After observing a putative CF- or PF-evoked CaT, the dendrite where the CaT was observed was magnified and a path for line scans (rate of 0.5 or 1 kHz) was drawn along the dendrite. Scans were triggered on 2–4 consecutive electrophysiology sweeps. Line scan sweeps from each recording were aligned using the peaks of the fluorescence profile of the Alexa 594 (red) channel to correct for drift using custom MATLAB scripts[22]. The aligned images were analyzed individually and averaged. CaTs are shown as ΔG/R and calculated using:

$$\Delta G/R = (G\text{-}G_0)/R$$

where $G_0$ is equal to the average Fluo-5F fluorescence preceding stimulation (170 ms), G is the magnitude of Fluo-5F fluorescence at a given time and R is Alexa 594 fluorescence. ΔG/R was calculated along the length of every line scan in a sweep. ΔG/R as a function of time was calculated from the average ΔG/R of the ten pixels surrounding the spatial peak of the CaT.

### Two-photon laser uncaging

Synaptic sites for glutamate uncaging were localized via 2P $Ca^{2+}$ imaging of locally recruited PF-MLI synapses, while making whole-cell voltage-clamp recordings. MLIs were filled with a morphological marker (Alexa 594; 30 µM) as well as a $Ca^{2+}$ indicator (Fluo-5F; 200 µM) to allow precise localization of activated synapses on MLI dendrites. PF-MLI synapses were recruited as described above[22]. In brief, PF-MLI synapses were recruited using paired-pulse (100 Hz) stimulation delivered by a theta-glass stimulating electrode placed near the recording site in the molecular layer. After allowing the dyes to fill the cell for

approximately 10 min, MLI dendrites were visually inspected while imaging at 2–5 Hz to find sites of increased fluorescence coincident with PF stimulation. These dendrites were then imaged via line scans (500 Hz) to determine the locus of $Ca^{2+}$ influx. To ensure uncaging was performed as close as possible to the postsynaptic site, five points were chosen surrounding the site of $Ca^{2+}$ influx (spaced by approximately 0.5 µm) and uncaging of MNI-glutamate (5 mM) was performed successively at each point to determine the site where (1) uEPSC was maximized; (2) rise time was minimized; and (3) decay time was minimized (Extended Data Fig. 6). Uncaging was then performed at this point while holding the cell at $V_h$ = −60 mV, 0 mV and +40 mV. At each holding potential uncaging was performed directly adjacent to the cellular membrane and at a distance of 0.5 µm or with lower laser power to reduce the concentration of uncaged glutamate detected by the postsynaptic receptors. Six to nine uEPSCs were averaged at each holding potential at each distance. Uncaging was performed using a tunable Coherent Chameleon Ultra II Ti:Sapphire laser set to 720 nm. Uncaging laser pulses were 0.3 ms in duration.

### Analytical resolution and signal-to-noise considerations

To ensure adequate analytical resolution, all analyses were evaluated with respect to signal-to-noise ratio rather than EPSC amplitude alone. For each experiment, baseline noise was quantified from pre-stimulus intervals, and analyses were restricted to EPSCs exceeding 3 × s.d. of baseline noise. Under these criteria, EPSCs in all datasets remained well above noise, including experiments in which EPSC amplitude was experimentally reduced. Currents were digitized at 15–50 kHz, and peak EPSC amplitude was quantified as the mean current within a ±100-µs window centered on the peak. At 50 kHz, this window comprises ~11 samples and reduces point-to-point baseline noise by √N. After averaging 10–20 sweeps, a baseline s.d. of ~2 pA corresponds to an effective s.d. of ~0.6 pA for peak-amplitude measurements. For each dataset (Extended Data Fig. 10), the relationship between EPSC amplitude and all measured parameters (RI, unitary conductance, kinetics, pharmacological sensitivity and $Ca^{2+}$ signaling) was examined to confirm that conclusions were not driven by signal size or limited analytical resolution.

### Numerical simulations

To simulate the changes in rectification of the AMPAR with glutamate, a Markov model of the AMPAR (Fig. 8a) was developed using Axograph and verified with Berkeley Madonna. Details and rates used are given in Results and in Fig. 8.

### Statistical analysis

Data were analyzed using Axograph X. Calculations and graphs were prepared with Microsoft Excel and Prism (GraphPad Software). Values are reported as mean ± s.e.m. and the statistical test used for each dataset is listed in the figure legends and/or Source Data. No statistical methods were used to predetermine sample sizes but our sample sizes are similar to those reported in previous publications[22]. Data distribution was assumed to be normal. When data were not appropriate for parametric analysis, nonparametric tests were used as indicated in the figure legends. Data collection and analysis were not performed blind to the conditions of the experiments. Randomization was not applicable because experimental groups were defined by genotype, input pathway, recording configuration, or pharmacological condition. Where possible, paired comparisons were made within the same cell or patch, and stimulus conditions were interleaved or repeated within recordings as appropriate. Each data point represents one cell or outside-out patch; paired values came from the same sample and were not counted as independent replicates. No animals were excluded from the analyses. Data points or recordings were excluded only if recordings failed predefined quality-control criteria (such as including changes in series resistance >20% or membrane rupture during perforated patch recordings), as described above. Means were compared using paired or unpaired two-tailed *t*-tests or ANOVAs with post hoc comparison tests. The criteria for statistical significance were $P < 0.05$.

### Reporting summary

Further information on research design is available in the Nature Portfolio Reporting Summary linked to this article.

## Data availability

All data supporting the results are included in the figures and Source Data Files. Source data are provided with this paper.

## Code availability

Custom scripts used in the present study can be downloaded from GitHub at https://github.com/rpennock/-Glutamate-AMPAR-tuning-manuscript and Zenodo at https://doi.org/10.5281/zenodo.21224276 (ref. 79).

## References

74. Konnerth, A., Llano, I. & Armstrong, C. M. Synaptic currents in cerebellar Purkinje cells. *Proc. Natl Acad. Sci. USA* **87**, 2662–2665 (1990).
75. Rae, J., Cooper, K., Gates, P. & Watsky, M. Low access resistance perforated patch recordings using amphotericin B. *J. Neurosci. Methods* **37**, 15–26 (1991).
76. Kennedy, W. M. & Overstreet-Wadiche, L. in *The Handbook of Electrophysiology: A Practical Guide for Neurophysiologists* (eds Duguid, I., Scimemi, A. & Wanaverbecq, N.) Ch. 3.4 (World Scientific Publishing, 2026).
77. Goldberg, J., Tamas, G., Aronov, D. & Yuste, R. Calcium microdomains in aspiny dendrites. *Neuron* **40**, 807–821 (2003).
78. Soler-Llavina, G. & Sabatini, B. Synapse-specific plasticity and compartmentalized signaling in cerebellar stellate cells. *Nat. Neurosci.* **9**, 798–806 (2006).
79. Pennock, R. L. rpennock/-Glutamate-AMPAR-tuning-manuscript: [Glutamate] tuning of AMPARs scripts. *Zenodo* https://doi.org/10.5281/zenodo.21224276 (2026).

## Acknowledgements

We thank all members of the Wadiche and Overstreet-Wadiche laboratories for their help. We appreciate the technical support from Mary Seelig. The authors also thank A. Plested, A. Tzingounis, J. Clements and C. E. Jahr for contributions to this project.

## Author contributions

Conceptualization: L.T.C., G.B., R.L.P., L.O.-W. and J.I.W. Formal analysis: G.B., L.T.C., R.L.P., X.Y., G.N.S., L.O.-W. and J.I.W. Funding acquisition: L.O.-W. and J.I.W. Investigation: G.B., L.T.C., R.L.P., X.Y., G.N.S. and J.I.W. Methodology: G.B., L.T.C., R.L.P. and J.I.W. Visualization: G.B., L.T.C., R.L.P., X.Y., G.N.S., L.O.-W. and J.I.W. Writing original draft L.T.C., L.O.-W. and J.I.W. Writing review & editing G.B., L.T.C., R.L.P., X.Y., G.N.S., L.O.-W. and J.I.W.

## Funding

This research was supported by funding from the National Institutes of Health (R01NS113948 to J.I.W. and R01NS064025 to L.O.-W.).

## Competing interests

The authors declare no competing interests.

## Additional information

**Extended data** is available for this paper at https://doi.org/10.1038/s41593-026-02414-w.

**Supplementary information** The online version contains supplementary material available at https://doi.org/10.1038/s41593-026-02414-w.

**Correspondence and requests for materials** should be addressed to Linda Overstreet-Wadiche or Jacques I. Wadiche.

**Peer review information** *Nature Neuroscience* thanks the anonymous reviewer(s) for their contribution to the peer review of this work.

https://doi.org/10.1038/s41593-026-02414-w

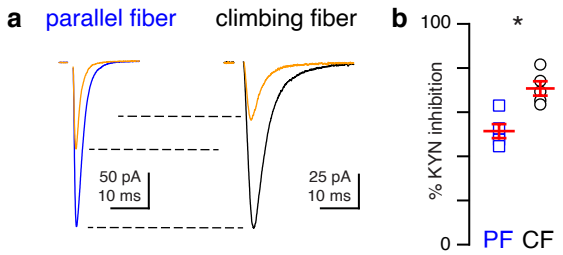


**Extended Data Fig. 1 | Different [glutamate] mediating PF- and CF-EPSCs.** **(a)** Representative PF- and CF-EPSCs before (blue or black) and after (orange) application of kynurenic acid (KYN; 500 µM). **(b)** KYN inhibited CF-EPSCs more than PF-EPSCs indicating a lower [glutamate] transient underlying CF-EPSCs (CF: 70.8 ± 3.3 % and PF: 51.5 ± 3.2 % of control, $n = 5$ each, $P = 0.0028$, two-tailed unpaired t-test). For all panels, summary data are mean ± SEM and Source data are provided in the Source Data File Extended Data Fig. 1.

https://doi.org/10.1038/s41593-026-02414-w

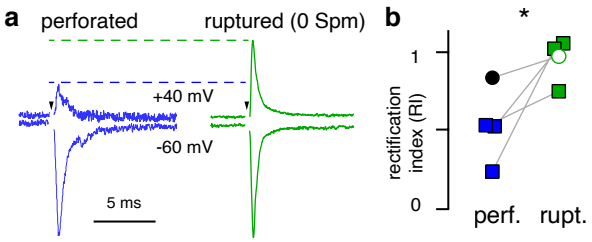


**Extended Data Fig. 2 | Perforated patch and rupture. (a)** Scaled average PF-EPSCs (-60 mV and +40 mV) recorded in the perforated patch configuration (blue traces) before and following patch rupture in whole-cell configuration (green) with an intracellular solution with 0 mM Spm and Amphotericin B (300 µg/ml). Dotted lines indicate the predicted amplitude for an ohmic (linear) response. **(b)** Summary of rectification Index (RI) of PF-EPSCs in the perforated patch configuration (blue squares) and CF-EPSC (black circle) before and following perforated patch rupture ($n = 4$; $P = 0.0331$, one-tailed t-test). The rectification index of PF- and CF-EPSCs following patch rupture (RI = 0.95 ± 0.07) is not different from an ohmic response (RI = 1, $P = 0.87$, Wilcoxon signed rank test). Note: Perforated patch rupture was also monitored with Alexa 594 dye. Source data are provided in the Source Data File Extended Data Fig. 2.

https://doi.org/10.1038/s41593-026-02414-w

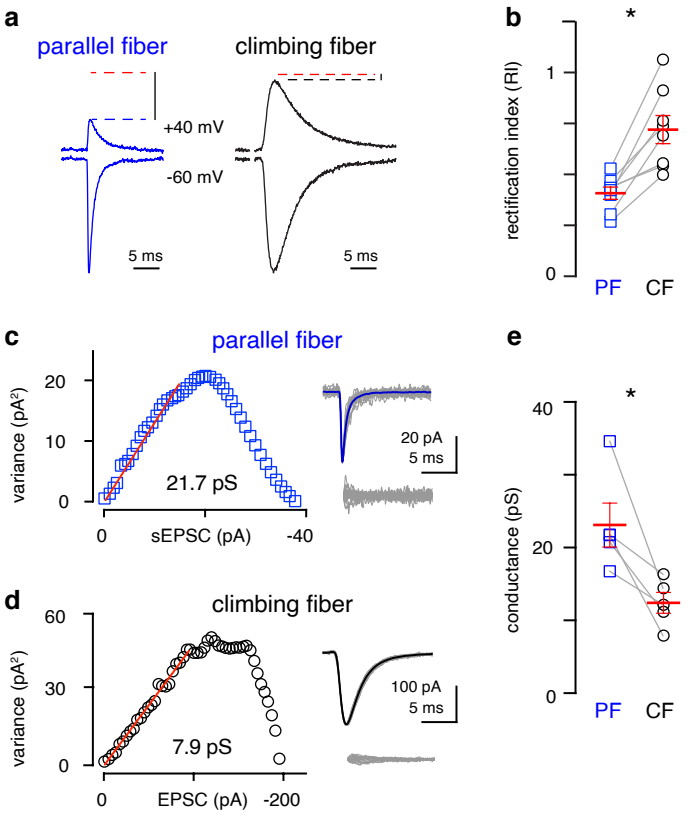


**Extended Data Fig. 3 | Rectification index differences persist at near-physiological (1.5 mM) $Ca^{2+}$. (a)** Example average sEPSCs (PF, blue) and CF- (black) EPSCs at -60 mV and +40 mV. Red dotted line indicates the predicted amplitudes for an ohmic (linear) response. **(b)** Summary of rectification index (RI) of PF- (0.41 ± 0.03, *n* = 8, blue squares) and CF-EPSCs (0.72 ± 0.07, *n* = 8, black circles; *P* = 0.001, two-tailed paired t-test). **(c - d)** Representative variance-mean plots of PF-sEPSCs (blue squares, linear fit = 21.7 pS) and CF-EPSCs (black circles, linear fit = 7.9 pS) and corresponding average response, individual sweeps (20 sweeps; gray) with difference currents (scaled average waveform minus each sweep). **(e)** Summary of PF (blue squares, 23.1 ± 3.0 pS) and CF (black circles, 12.4 ± 1.4 pS) unitary conductance (n = 5; *P* = 0.0205, two-tailed paired t-test). For all panels, summary data are mean ± s.e.m. and Source data are provided in the Source Data File Extended Data Fig. 3.

https://doi.org/10.1038/s41593-026-02414-w

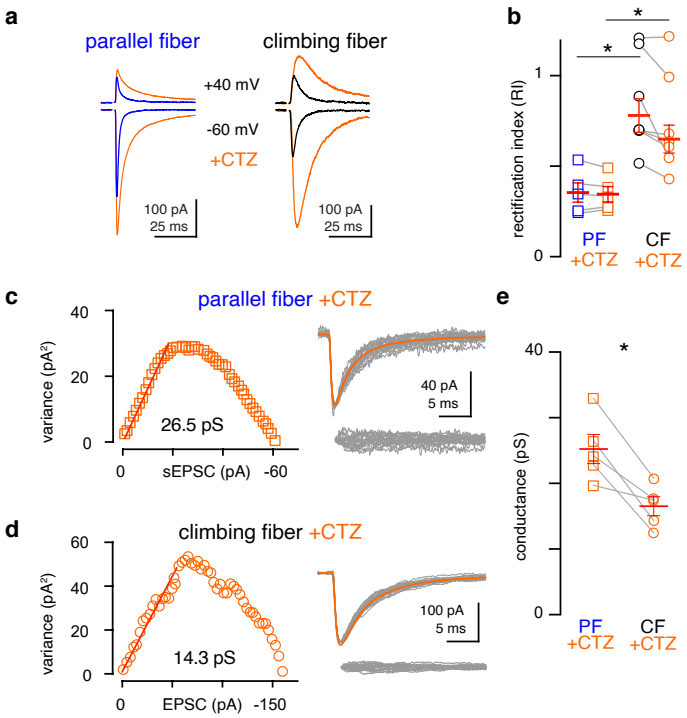


**Extended Data Fig. 4 | AMPAR desensitization does not contribute to PF- and CF-EPSC rectification index differences. (a)** Representative PF- (blue) and CF-EPSCs (black) at -60 and +40 mV in the absence and presence of cyclothiazide (orange, CTZ, 100 µM). At -60 mV, CTZ did not significantly affect the amplitude of PF-EPSCs 129.8 ± 10.0% (n = 5, $P = 0.0625$, Wilcoxon Signed Rank test) and potentiated CF-EPSCs to 233.6 ± 56.3% of control (n = 7; $P = 0.0156$, Wilcoxon Signed Rank test). **(b)** Summary of CTZ effect on rectification Index (RI). PF: 0.35 ± 0.05 & PF in CTZ: 0.35 ± 0.04; n = 5 and CF: 0.84 ± 0.12 & CF in CTZ: 0.74 ± 0.13 n = 7; Two-way ANOVA; $P = 0.0001$ for the pathway (PF & CF). Uncorrected Fisher's least significant difference tests (PF vs CF $P = 0.0014$; PF CTZ vs CF CTZ $P = 0.0079$). **(c - d)** Representative variance-mean plots in CTZ of PF-sEPSCs (orange squares, linear fit = 26.5 pS) and CF-EPSCs (orange circles, linear fit = 14.3 pS) and corresponding average response, individual sweeps (20 sweeps; gray) with difference currents (scaled average waveform minus each sweep). **(e)** Summary of PF (orange squares, 25.2 ± 2.2 pS) and CF (orange circles, 16.5 ± 1.4 pS) unitary conductance in the presence of CTZ (n = 5; $P = 0.0102$, two-tailed paired t-test). For all panels, summary data are mean ± s.e.m. and Source data are provided in the Source Data File Extended Data Fig. 4.

https://doi.org/10.1038/s41593-026-02414-w

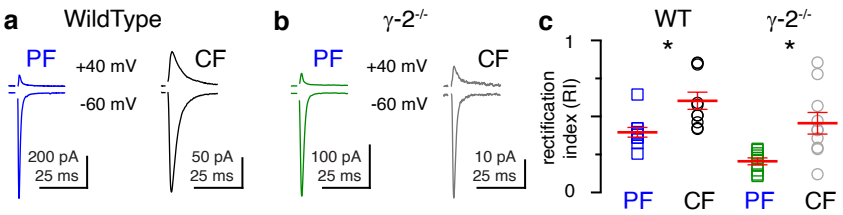


**Extended Data Fig. 5 | TARP γ-2 does not contribute to PF- and CF-EPSC RI differences. (a - b)** Representative PF- (blue and green) and CF- (black and gray) EPSCs from WT and TARP γ-2 KO littermates at -60 mV and +40 mV.**(c)** Summary of rectification Indices (RIs) WT: PF 0.40 ± 0.03 (n = 10) and CF: 0.60 ± 0.05 (n = 10) and TARP γ-2 KO: PF: 0.19 ± 0.03 (n = 10) and CF: 0.45 ± 0.07 (n = 11). Two-way ANOVA; $P = < 0.0001$ for the pathway (PF & CF) and $P = 0.0007$ for the genotype (PF γ-2 KO & CF γ-2 KO). Uncorrected Fisher's least significant difference tests (PF vs PF γ-2 KO $P = 0.0054$; CF vs CF γ-2 KO $P = 0.0296$). For all panels, summary data are mean ± s.e.m. and Source data are provided in the Source Data File Extended Data Fig. 5.

https://doi.org/10.1038/s41593-026-02414-w

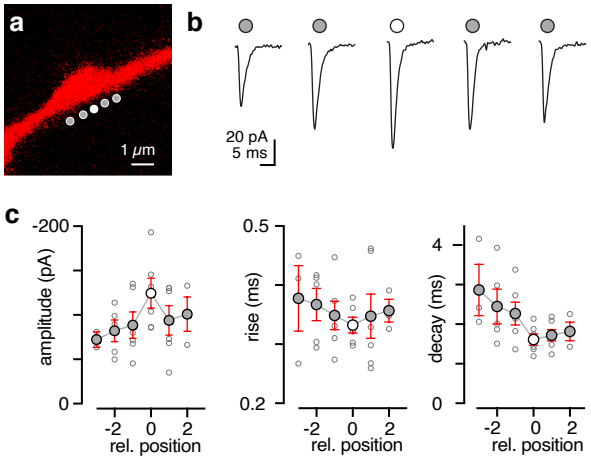


**Extended Data Fig. 6 | 2 PLU mapping of AMPARs. (a)** 2P magnified image of a putative postsynaptic density of an MLI filled with Alexa 594. Uncaging spots are represented by gray and white circles. **(b)** uEPSCs (-60 mV) from corresponding uncaging spots shown in (A). **(c)** Summary data for amplitude, rise (20–80%) and decay time (single exponential) of uEPSCs, representing pooled data from Fig. 2d, e uncaging experiments from 3–6 uncaging spots (average of 5) across putative receptor clusters (n = 6 neurons). This illustrates how we map the "optimal" location for uncaging prior to every uncaging experiment. For all panels, summary data are mean ± s.e.m. and Source data are provided in the Source Data File Extended Data Fig. 6.

https://doi.org/10.1038/s41593-026-02414-w

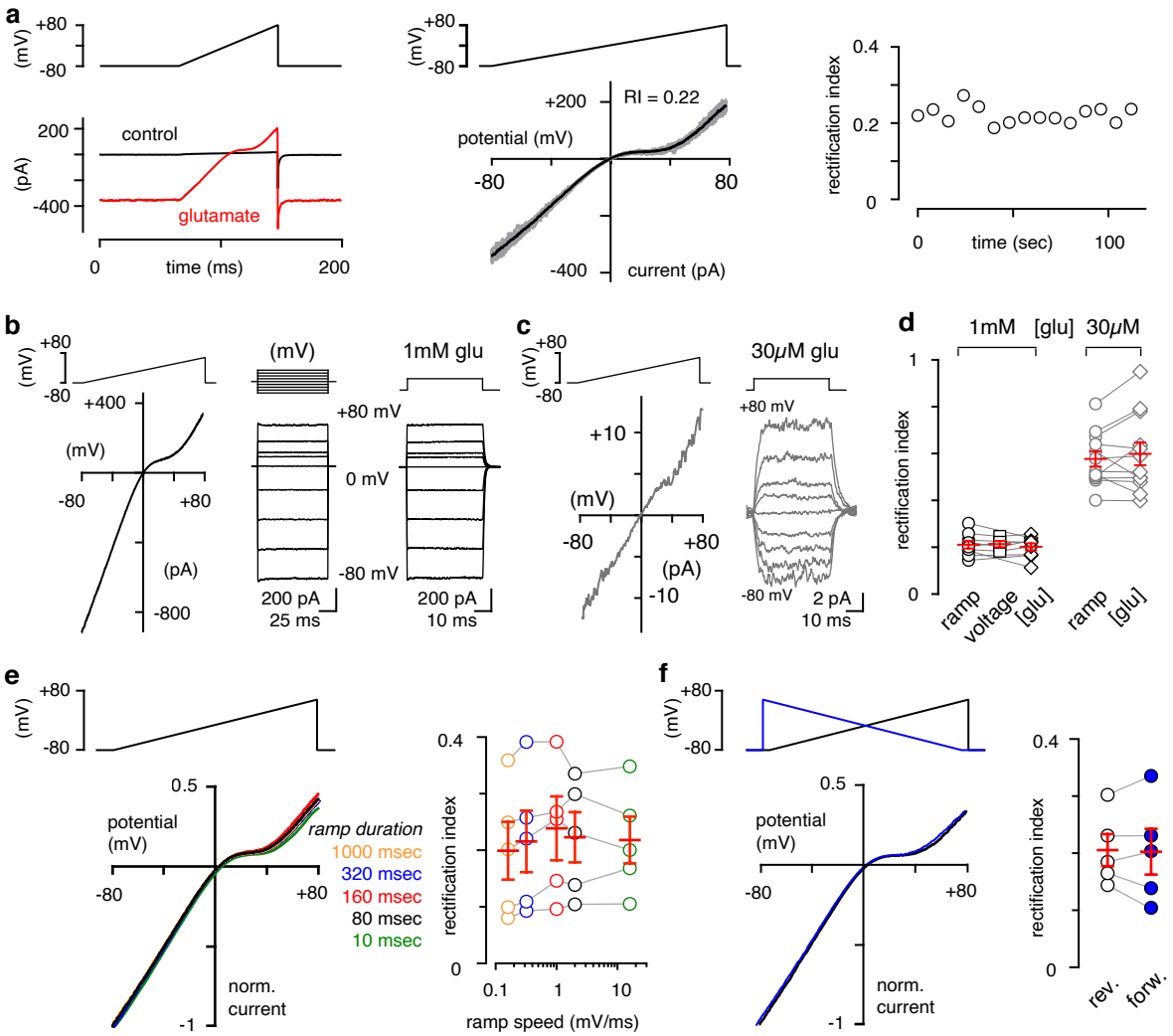


**Extended Data Fig. 7 | AMPAR rectification assay. (a)** Ramp protocol (top) and corresponding currents (bottom) in control (black) or in 10 mM glutamate (red). Ramp protocol (center top) and individual subtracted current responses (center bottom,15 sweeps in gray) with average response (black). Plot of rectification index vs time showing stability is shown on right panel. **(b)** Representative currents following voltage ramp (left), voltage jumps (center), and concentration jumps (right) to the same o/o MLI patch (1 mM glutamate). **(c)** Representative currents following voltage ramp (left), and concentration jumps to the same o/o patch (30 μM glutamate). **(d)** Summary from (**b**) and (**c**). Rectification index 1 mM glutamate: ramp protocol (0.22 ± 0.02, n = 9), voltage jump protocol (0.21 ± 0.01, n = 9) and concentration jump protocol (0.2 ± 0.01, n = 4) are not different (One-Way ANOVA, $P = 0.80$). Rectification index 30 μM glutamate: ramp (0.58 ± 0.03, n = 12) and concentration (0.60 ± 0.05, n = 12) are not different ($P = 0.71$, two-tailed paired t-test). **(e)** The speed (and duration) of voltage ramps (10 - 1000 ms; 16 - 0.16 mV/ms) does not affect rectification index (1 mM glutamate; 16 mV/ms: 0.22 ± 0.04, 2 mV/ms: 0.22 ± 0.04, 1 mV/ms: 0.23 ± 0.05, 0.32 mV/ms: 0.21 ± 0.05, 0.16 mV/ms: 0.20 ± 0.05; n = 5 each, $P = 0.23$, One-way ANOVA). **(f)** The direction of the ramp at 2 mV/ms does not affect rectification index (1 mM glutamate; reverse: 0.21 ± 0.03 and forward: 0.20 ± 0.04; n = 5, $P = 0.9187$, two-tailed paired t-test). IV plots in (e) and (f) are normalized to -80 mV. All currents are recorded in the presence of CTZ (100 μM). For all panels, summary data are mean ± s.e.m. and Source data are provided in the Source Data File Extended Data Fig. 7.

https://doi.org/10.1038/s41593-026-02414-w

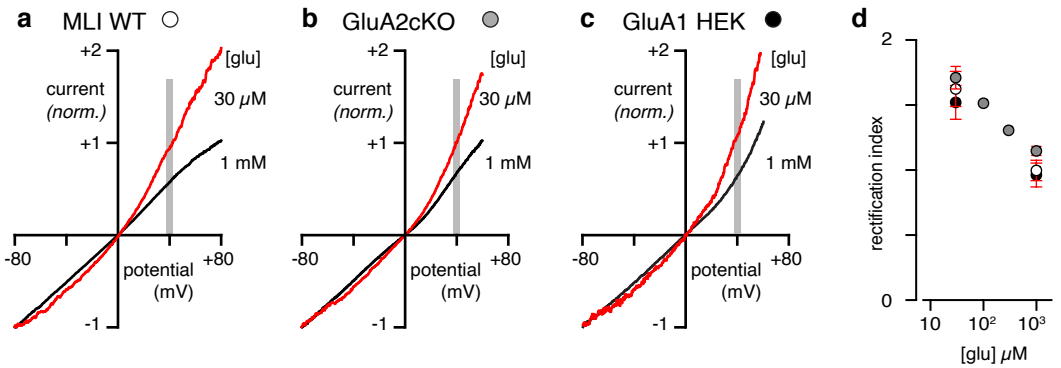


**Extended Data Fig. 8 | Intrinsic outward rectification of o/o patches with nominal spermine. (a-c)** Normalized glutamate-dependent voltage ramps (1 mM and 30 μM) without spermine ( + ATP) from WT MLIs **(a)**, GluA2cKO MLIs **(b)**, and HEK cells expressing GluA1 **(c)**. **(d)** Summary data of rectification index as a function of [glutamate] from MLI (white circles), GluA2cKO (gray circles), and GluA1 HEK (black circles) o/o patches with 0 μM spermine and ATP. The rectification index as a function of [glutamate] from MLI WT o/o patches with 0 μM spermine and 4 mM MgATP (white circles): 30 μM glutamate: 1.6 ± 0.1 (n = 5); 1 mM glutamate: 1.0 ± 0.08 (n = 5). The glutamate-dependent rectification index from GluA2cKO o/o patches with 20 mM $Na_2ATP$ at 30 μM glutamate: 1.83 ± 0.06 (n = 3); 100 μM glutamate: 1.5 (n = 1); 300 μM glutamate: 1.3 (n = 1); 1 mM glutamate: 1.23 ± 0.02 (n = 4). The glutamate-dependent rectification index from GluA2cKO o/o patches with 4 mM MgATP at 30 μM glutamate: 1.7 ± 0.1 (n = 9); 1 mM glutamate: 1.1 ± 0.04 (n = 9). Graph shows combined 4 mM and 20 mM ATP (gray circles). The rectification index as a function of [glutamate] from GluA1 HEK o/o patches with 0 μM spermine and 4 mM MgATP (black circles): 30 μM glutamate: 1.5 ± 0.13 (n = 7); 1 mM glutamate: 0.96 ± 0.09 (n = 7). Summary data are mean ± s.e.m. and Source data are provided in the Source Data File Extended Data Fig. 8.

https://doi.org/10.1038/s41593-026-02414-w

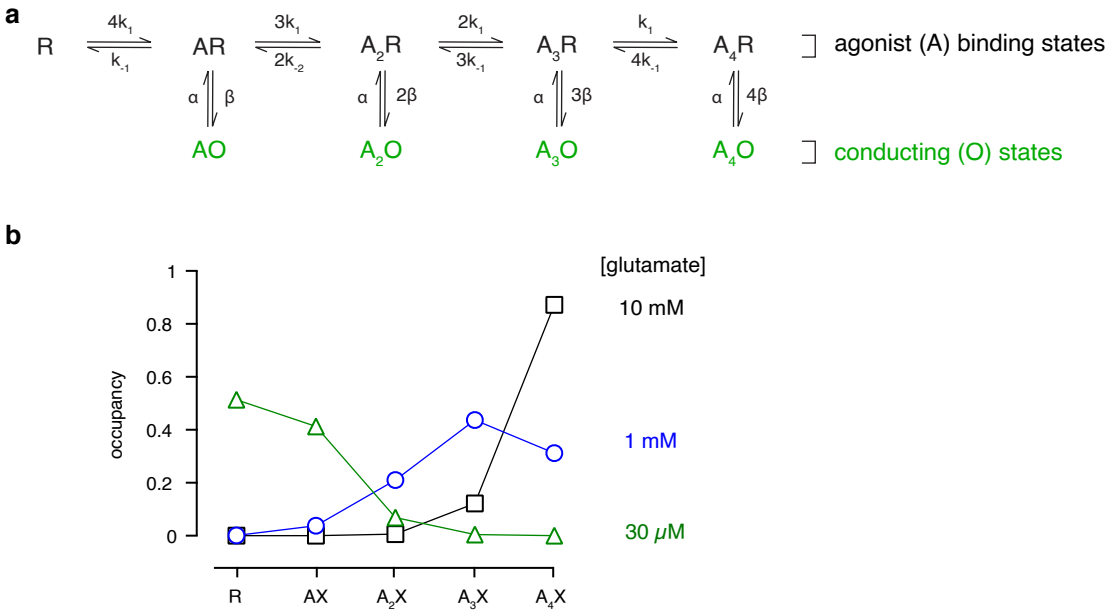


**Extended Data Fig. 9 | Closed and open state occupancies depend on [glutamate]. (a)** Kinetic scheme of agonist (glutamate) binding to four independent subunits in the absence of internal polyamine (Spermine). Rates are as in Fig. 8. Units are $M^{-1} s^{-1}$ (for $k_1$) or $s^{-1}$. $k_1$ is dependent on [glutamate]. **(b)** Unbound (R) and occupancies with one (AR + AO), two ($A_2R + A_2O$), three ($A_3R + A_3O$), or four ($A_4R + A_4O$) ligands at 30 µM (green), 1 mM (blue), and 10 mM (black) glutamate. Source data are provided in the Source Data File Extended Data Figure 9.

https://doi.org/10.1038/s41593-026-02414-w

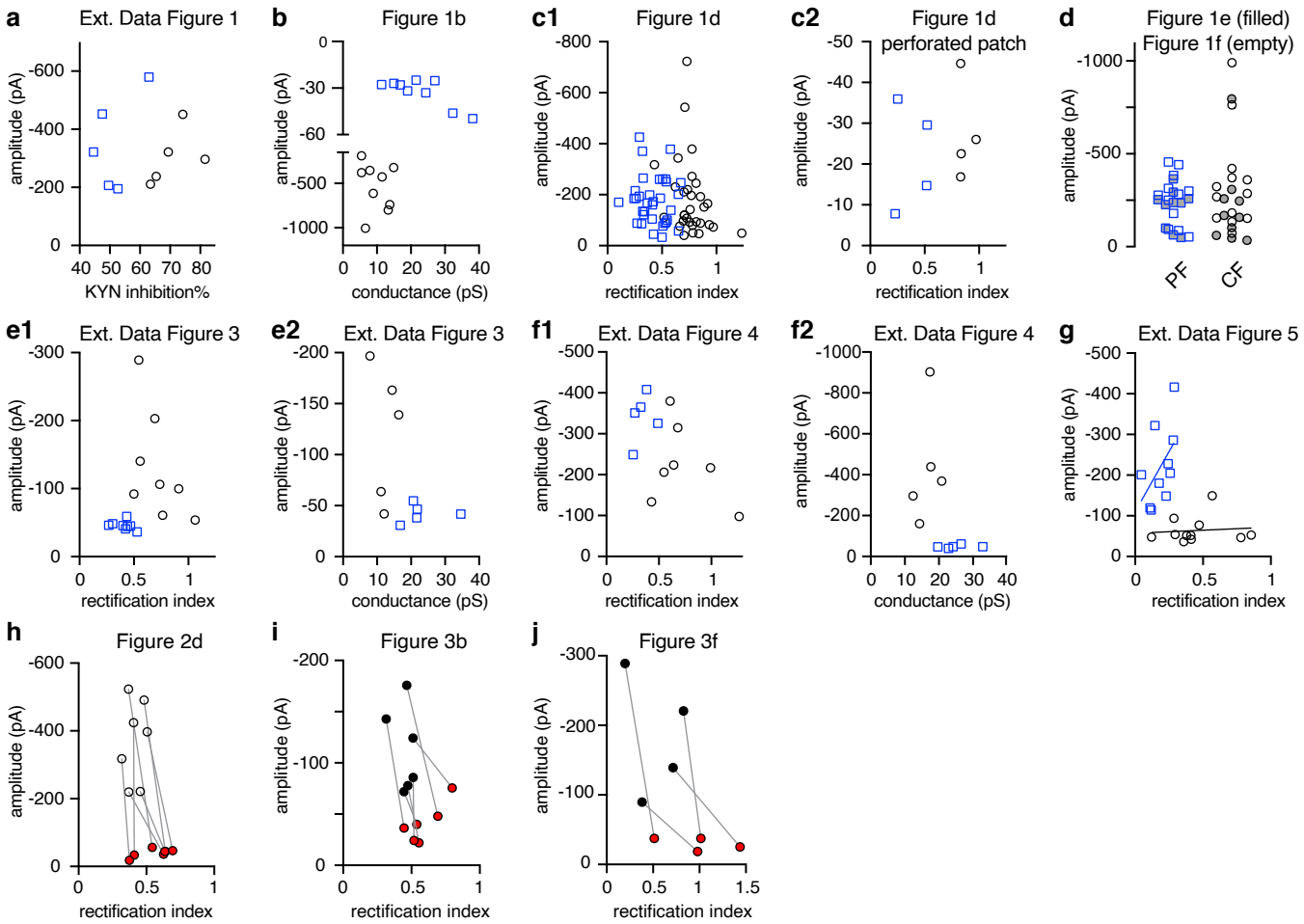


**Extended Data Fig. 10 | Relationships between EPSC amplitudes and synaptic metrics. (a)** EPSC amplitude plotted against inhibition by kynurenic acid for evoked PF- (blue squares) and CF-EPSCs (black circles). PF- and CF-EPSC amplitudes are comparable (PF: −351.1 ± 73.7 pA; CF: −303.6 ± 41.9 pA; n = 5 each; $P = 0.5943$, two-tailed unpaired t-test), yet inhibition differs between inputs indicating that differences in antagonist sensitivity are not explained by signal size. See Extended Data Fig. 1. **(b)** EPSC amplitude plotted against estimated unitary conductance for spontaneous PF-EPSCs (blue squares) and evoked CF-EPSCs (black circles) recorded in the same cells. As expected, spontaneous PF events are smaller than evoked CF-EPSCs; however, they show higher estimated conductance, demonstrating that differences in analytical resolution at low amplitudes do not account for the observed conductance estimates. See Fig. 1b. **(c1)** Rectification index plotted against EPSC amplitude for PF- (blue squares) and CF-EPSCs (black circles). PF- and CF-EPSCs have similar amplitudes (PF: 178.2 ± 16.2 pA, n = 34; CF: 181.6 ± 27.3 pA, n = 31; $P = 0.8902$, two-tailed unpaired t-test), yet rectification differs between inputs. See Fig. 1d. **(c2)** Rectification index plotted against EPSC amplitude for perforated patch EPSCs (< 50 pA), demonstrating PF (blue squares) vs CF (black circles) differences under low-signal conditions. See Fig. 1d. **(d)** EPSC amplitude versus percent inhibition for NASPM experiments (filled symbols denote paired PF and CF recordings). PF- (blue squares) and CF-EPSC (black circles) amplitudes overlap (PF: −199.6 ± 32.7 pA; CF: −208.7 ± 70.9 pA; n = 10; $P = 0.8946$, two-tail unpaired t-test), whereas inhibition differs significantly indicating that NASPM sensitivity is not determined by EPSC size. See Fig. 1e, f. **(e1)** Rectification index plotted against EPSC amplitude for PF sEPSCs (blue squares) and CF-EPSCs (black circles) recorded in 1.5 mM Ca2 + . As expected, PF sEPSCs are smaller than CF-EPSCs; however, rectification differs between inputs. See Extended Data Fig. 3. **(e2)** Unitary conductance plotted against EPSC amplitude for PF (blue squares) and CF (black circles) responses, demonstrating that PF versus CF differences in conductance are preserved in 1.5 mM Ca2 + . See Extended Data Fig. 3. **(f1)** Rectification index plotted against EPSC amplitude for PF- (blue squares) and CF-EPSCs (black circles) recorded in the presence of CTZ. Rectification differs between inputs across the observed amplitude range. See Extended Data Fig. 4. **(f2)** Unitary conductance plotted against EPSC amplitude for spontaneous PF-EPSCs (blue squares) and evoked CF-EPSCs (black circles) recorded in the same cells. As expected, PF sEPSCs are smaller than evoked CF-EPSCs; nevertheless, PF vs. CF differences in conductance are preserved. See Extended Data Fig. 4. **(g)** EPSC amplitude versus rectification index in interneuron-specific TARP γ2 knockout recordings. Rectification index does not correlate with EPSC amplitude for either PF- (blue squares, $P = 0.131$, Linear regression) or CF-EPSCs (black circles, $P = 0.774$, Linear regression), indicating that rectification measurements are not driven by EPSC size. See Extended Data Fig. 5. **(h)** Paired PF-EPSC amplitude versus rectification index before (open black circles) and after (filled red circles) bafilomycin treatment. Bafilomycin reduces EPSC amplitude and increases rectification in paired recordings, consistent with reduced effective glutamate concentration rather than limitations in analytical resolution. See Fig. 2d. **(i)** uEPSC amplitude versus rectification index for glutamate uncaging at near (filled black circles) and far (filled red circles) distances. Increasing uncaging distance reduces uEPSC amplitude and increases rectification in paired measurements, consistent with reduced effective glutamate concentration. See Fig. 3b. **(j)** uEPSC amplitude versus rectification index for glutamate uncaging at high (filled black circles) and low (filled red circles) laser power. Decreasing laser power reduces uEPSC amplitude and increases rectification in paired measurements, consistent with reduced effective glutamate concentration. See Fig. 3f. Source data are provided in the Source Data File Extended Data Figure 10.

nature portfolio

Corresponding author(s): *Double-anonymous peer review submissions: write DAPR and your manuscript number here instead of author names.*

Last updated by author(s): *YYYY-MM-DD*

# Reporting Summary

Nature Portfolio wishes to improve the reproducibility of the work that we publish. This form provides structure for consistency and transparency in reporting. For further information on Nature Portfolio policies, see our Editorial Policies and the Editorial Policy Checklist.

## Statistics

For all statistical analyses, confirm that the following items are present in the figure legend, table legend, main text, or Methods section.

| n/a | Confirmed | |
|---|---|---|
| ☐ | ☒ | The exact sample size (*n*) for each experimental group/condition, given as a discrete number and unit of measurement |
| ☐ | ☒ | A statement on whether measurements were taken from distinct samples or whether the same sample was measured repeatedly |
| ☐ | ☒ | The statistical test(s) used AND whether they are one- or two-sided<br>*Only common tests should be described solely by name; describe more complex techniques in the Methods section.* |
| ☐ | ☒ | A description of all covariates tested |
| ☐ | ☒ | A description of any assumptions or corrections, such as tests of normality and adjustment for multiple comparisons |
| ☐ | ☒ | A full description of the statistical parameters including central tendency (e.g. means) or other basic estimates (e.g. regression coefficient) AND variation (e.g. standard deviation) or associated estimates of uncertainty (e.g. confidence intervals) |
| ☐ | ☒ | For null hypothesis testing, the test statistic (e.g. *F*, *t*, *r*) with confidence intervals, effect sizes, degrees of freedom and *P* value noted<br>*Give P values as exact values whenever suitable.* |
| ☒ | ☐ | For Bayesian analysis, information on the choice of priors and Markov chain Monte Carlo settings |
| ☒ | ☐ | For hierarchical and complex designs, identification of the appropriate level for tests and full reporting of outcomes |
| ☒ | ☐ | Estimates of effect sizes (e.g. Cohen's *d*, Pearson's *r*), indicating how they were calculated |

*Our web collection on statistics for biologists contains articles on many of the points above.*

## Software and code

Policy information about availability of computer code

| | |
|---|---|
| Data collection | Electrophysiological data were collected using pClamp 10 software (Molecular Devices). Imaging data were collected using Prairie View software (Bruker Corporation). |
| Data analysis | Electrophysiological and time series Ca2+ imaging data were analyzed using Axograph X software. Initial image inspection and processing was performed using ImageJ. Custom MATLAB scripts were used to align images, calculate time series data from line scans, and fit line scan images with Gaussian functions. Statistical testing and curve fitting was performed using Graphpad Prism 9.To simulate the changes in rectification of the AMPA receptor with glutamate, a Markov model of the AMPAR was developed using Axograph (Sydney, Australia) and verified with Berkeley Madonna (Berkeley, USA). |

For manuscripts utilizing custom algorithms or software that are central to the research but not yet described in published literature, software must be made available to editors and reviewers. We strongly encourage code deposition in a community repository (e.g. GitHub). See the Nature Portfolio guidelines for submitting code & software for further information.

## Data

Policy information about availability of data

All manuscripts must include a data availability statement. This statement should provide the following information, where applicable:

- Accession codes, unique identifiers, or web links for publicly available datasets
- A description of any restrictions on data availability
- For clinical datasets or third party data, please ensure that the statement adheres to our policy

Custom scripts used in the present study can be downloaded from https://github.com/rpennock/-Glutamate-AMPAR-tuning-manuscript

## Research involving human participants, their data, or biological material

Policy information about studies with human participants or human data. See also policy information about sex, gender (identity/presentation), and sexual orientation and race, ethnicity and racism.

| | |
|---|---|
| Reporting on sex and gender | n/a |
| Reporting on race, ethnicity, or other socially relevant groupings | n/a |
| Population characteristics | n/a |
| Recruitment | n/a |
| Ethics oversight | n/a |

Note that full information on the approval of the study protocol must also be provided in the manuscript.

# Field-specific reporting

Please select the one below that is the best fit for your research. If you are not sure, read the appropriate sections before making your selection.

☒ Life sciences ☐ Behavioural & social sciences ☐ Ecological, evolutionary & environmental sciences

For a reference copy of the document with all sections, see nature.com/documents/nr-reporting-summary-flat.pdf

# Life sciences study design

All studies must disclose on these points even when the disclosure is negative.

| | |
|---|---|
| Sample size | For comparisons of physiological and pharmacological properties sample sizes were selected based on what is common in this field of study. Effects were large and consistent between recordings, making large sample sizes unnecessary. |
| Data exclusions | 1) Experiments were discarded if series resistance (Rs) of the electrophysiological changed by >20% over the course of the experiment.<br><br>2) If post hoc analysis of evoked spillover (climbing fiber pathway) EPSCs revealed contamination of the signal by parallel fiber activation the recording was discarded.<br><br>3)During analysis of evoked synaptic (parallel fiber pathway) Ca2+ transients experiments were excluded if the location of the Ca2+ transient along the length of the dendrite changed. Such a change indicates that the original synaptic site is no longer being recruited and previously acquired baseline data is invalid. |
| Replication | Replicates of each experiment are indicated as the sample size 'n'. |
| Randomization | A mixture of male and female mice were used in all experiments. Randomization was not applicable because experimental groups were defined by genotype, input pathway, recording configuration, or pharmacological condition. Where possible, paired comparisons were made within the same cell or patch, and stimulus conditions were interleaved or repeated within recordings as appropriate. |
| Blinding | Blinding was not possible for these experiments as all experimental results can be observed in real time, and experiments were generally performed and analyzed by the multiple investigators. |

# Reporting for specific materials, systems and methods

We require information from authors about some types of materials, experimental systems and methods used in many studies. Here, indicate whether each material, system or method listed is relevant to your study. If you are not sure if a list item applies to your research, read the appropriate section before selecting a response.

## Materials & experimental systems

| n/a | Involved in the study |
|---|---|
| ☒ | ☐ Antibodies |
| ☐ | ☒ Eukaryotic cell lines |
| ☒ | ☐ Palaeontology and archaeology |
| ☐ | ☒ Animals and other organisms |
| ☒ | ☐ Clinical data |
| ☒ | ☐ Dual use research of concern |
| ☒ | ☐ Plants |

## Methods

| n/a | Involved in the study |
|---|---|
| ☒ | ☐ ChIP-seq |
| ☒ | ☐ Flow cytometry |
| ☒ | ☐ MRI-based neuroimaging |

# Eukaryotic cell lines

Policy information about cell lines and Sex and Gender in Research

| | |
|---|---|
| Cell line source(s) | HEK293 cells were purchased from ATCC (American Type Culture Collection; CRL-3216). |
| Authentication | Constructs used in heterologous expression of AMPARs were independently sequenced (GluA1 flip in pIRES-EGFP) |
| Mycoplasma contamination | n/a |
| Commonly misidentified lines (See ICLAC register) | The cell line was checked against the ICLAC database of commonly misidentified cell lines and was not listed. Cells were authenticated by ATCC prior to distribution; no additional authentication was performed for this study. |

# Animals and other research organisms

Policy information about studies involving animals; ARRIVE guidelines recommended for reporting animal research, and Sex and Gender in Research

| | |
|---|---|
| Laboratory animals | Male and female mice, age P16-38. PV-GluA2cKO mice were generated by crossing the parvalbumin PV-2A-Cre-D (#012358, Jackson Laboratory) with GluR-B2lox mice (gift from Rolf Sprengel, Max Planck Institute). Gamma-2 KO mice (#001756, Jackson Laboratory) were a gift from Susumu Tomita (Yale Medical University). |
| Wild animals | n/a |
| Reporting on sex | A mixture of male and female mice were used in this study, and sex differences were not considered during design of the experiment. |
| Field-collected samples | n/a |
| Ethics oversight | All experimental preparations were performed using protocols approved by the Institutional Animal Care and Use Committee of the University of Alabama at Birmingham |

Note that full information on the approval of the study protocol must also be provided in the manuscript.

# Plants

| | |
|---|---|
| Seed stocks | n/a |
| Novel plant genotypes | n/a |
| Authentication | n/a |